Adaptive isogeometric gear contact analysis: geometry generation, truncated hierarchical B-Spline refinement and validation

Christos Karampatzakis, Angelos Mantzaflaris, Christopher Provatidis, Athanasios Mihailidis

Adaptive isogeometric gear contact analysis: geometry generation, truncated hierarchical B-Spline refinement and validation

Christos Karampatzakis[a,1,*], Angelos Mantzaflaris[b], Christopher Provatidis[c], Athanassios Mihailidis[a]

[a] *School of Mechanical Engineering, Aristotle University of Thessaloniki, University Campus, Thessaloniki, 54124 Greece*
[b] *Centre Inria d'Université Côte d'Azur, 2004 route des Lucioles, B.P. 93, Sophia Antipolis, 06902, France*
[c] *School of Mechanical Engineering,National Technical University of Athens, 9 Iroon Polytechniou Str., Athens, 15780, Greece*

Abstract

Gears are one of the most widely used transmission components. Their operation relies on the contact between mating gear teeth flanks for the transmission of power. Accurate prediction of the contact stresses at these regions, is crucial for the design and dimensioning of these systems. Gear design is centered around highly smooth involute curves that greatly influence their contact behaviour. In this paper, a fully adaptive isogeometric contact modelling scheme, based on hierarchical splines, is presented and applied to the simulation of gear contact problems. In particular, isogeometric simulation is performed for the modelling of mating pair of gear teeth, regarded as linearly elastic bodies. A boundary fitted B-Spline representation of the teeth is automatically generated from engineering design parameters and is used to define the initial discretisation basis. The numerical integration over the contact region is addressed using the so called, Gauss-Point to Surface formulation and a closest point projection procedure. Truncated hierarchical B-Splines are used to capture the highly localised nature of contact, while effectively reducing the number of degrees of freedom. The adaptivity is driven by the strain energy density gradient, which allows to automatically localise the mesh without *a priori* knowledge of the contact region between the teeth flanks. In our experiments we justify the choices made in different steps of our algorithm and we assess the performance of our adaptive solver with respect to classical tensor product B-Splines.

Keywords: isogeometric analysis, contact mechanics, gears, local refinement, adaptivity, hierarchical splines

1. Introduction

A critical part in the design process of any mechanical assembly involving contacting parts, is the determination of the contact pressures developed during operation. This is especially true for mechanical transmission systems that use gears, since contact pressure is linked to major failure modes of gears, such as scuffing, pitting and spalling. The stresses developed at the contacting regions and the tooth's root are of critical importance for the determination of the gear's fatigue life both in terms of surface as well as bending fatigue [1, 2]. Another important aspect is the deformation of the gear under this pressure load, which introduces transmission errors that cause excitations and lead to higher noise levels during operation [3].

Tooth contact analysis (TCA) is the umbrella term used to encompass all methodologies that simulate the meshing of gears. Through numerical modelling, key performance characteristics of the pair can be assessed and thus costly prototyping can be reduced to a minimum [4]. Based on a properly chosen contact model, valuable engineering data such as mesh stiffness, transmission error, contact pattern and much more

*Corresponding author
Email addresses: karampatzakis@meng.auth.gr (Christos Karampatzakis), angelos.mantzaflaris@inria.fr (Angelos Mantzaflaris), cprovat@central.ntua.gr (Christopher Provatidis), amih@meng.auth.gr (Athanassios Mihailidis)

can be calculated [5, 6] and subsequently microgeometry modifications [7] can be introduced to the tooth profile in order to optimise performance. For that reason many methods have been used in practice to determine the pressure field of contacting bodies. The oldest among them is the analytical solution introduced by Heinrich Hertz [8]. His theory assumes contact between two elastic, infinite half-spaces of constant curvature, with small deformations and provides an analytical solution for the pressure exerted between the bodies. Even though these idealised assumptions do not always hold, his theory is widely used to this day in contact analysis. Another more recent approach is that of the elastic foundation method [9]. In this, a body is assumed to be a collection of independent linear spring elements. This assumption neglects the influence of one element on its neighbors, yet it has been applied in practice since it is a computationally inexpensive method, compared to more elaborate ones. The dominant method for tooth contact analysis is the Finite Element Method (FEM). Contact simulation with the FEM has been widely studied and is used in numerous practical applications. It is a very flexible method that can model arbitrary geometries and various material models and manages to provide good results. This performance comes at the cost of increased computational effort, compared to the aforementioned methods. Its shortcomings do not end there though. In the FEM, the part is modelled as a collection of elements of C^0 continuity and typically of first order. This introduces geometrical errors, especially when considering the deformed configuration, although accuracy of geometry is of utmost importance for contact simulations.

More recently, a new simulation paradigm has been developed, culminating the trend of macroelements [10] that started in the 1980's, namely Isogeometric Analysis (IGA) [11]. IGA contrary to the FEM, uses the spline family of basis functions. This is the same basis used in most commercial Computer Aided Design (CAD) software and thus no discretisation with Lagrange elements is performed in the transition from design to analysis, as in the FEM. This new approach offers many favourable attributes, especially for contact modelling. which have been known already from the seminal paper on IGA by Hughes et al. [11]. First and foremost, the contacting bodies are represented "exactly", or at least as well as their CAD representation admits, and they are not tessellated as is the case with the FEM. Thus no geometric error is introduced in the transition from the model used in design to the one used in analysis. The higher continuity of the basis gives rise to a continuous and smooth displacement field which is very advantageous for large deformation contact, since the parts remain smooth even under large deformation. Furthermore it ensures that there are continuous tangent and normal vector fields defined for every point of the surface, which is essential for contact computations and closest point projection. This eliminates the need for special smoothing techniques commonly employed for FE contact modelling [12]. The basis also possesses the non-negativity and variation diminishing properties, which are desirable when working with parametrisations of higher degree.

Many different isogeometric contact formulations have been developed, or adapted from the FEM. They have been thoroughly summarised in the review paper [13]. More recently in [14] the authors have not only reviewed the advancements in the field of isogeometric contact analysis, but also its application to various fields of engineering. Previously in [15] we have explored the performance of standard tensor B-Splines compared to linear Lagrange elements in the modelling of gear teeth contact. The spline basis was shown to achieve the same level of accuracy with the classical FEM discretization basis, with less degrees of freedom and lower computation times. Furthermore, the studies performed in [16, 17] have applied isogeometric analysis based on tensor product (TP) B-Splines to the modelling of contacting gear teeth, in two and three dimensional settings, respectively. They have showcased that IGA achieves very good performance with respect to equivalent FEM simulations performed in an established commercial solver. Moreover, isogeometric analysis has been coupled with a meshless method and applied to contacting gears in [18]. There, the authors combined the favourable characteristics of IGA in the contact modelling while avoiding the creation of a structured discretisation for the bulk of the gears with a meshfree method.

In many applications contact is highly localised, therefore it is paramount to consider local refinement of the solution space, in order to achieve accurate enough results. Refinement using standard tensor product splines suffers from unwanted propagation away from the domain of interest as well as from badly-shaped elements, therefore more sophisticated spline constructions that allow for truly local refinement should

be used. In [19] *a priori* refined hierarchical splines were used to model frictionless contact phenomena in both small and large deformations setting. The authors made use of a normalised version of the hierarchical basis in order to retrieve the partition of unity. Similarly the authors of [20], used another locally refinable construction from the family of splines, namely *a priori* refined T-Splines [21], in order to accurately resolve the contact region. Again, the results are compared to the ones obtained with NURBS discretisations as well as with analytical solutions for benchmark problems and a very good agreement is achieved. Nevertheless, both of the aforementioned studies refrain from using local adaptivity procedures and thus do not fully exploit the potential of these spline constructions. Adaptivity allows for the automatic refinement of the basis, based on the results of a previous simulation, thus not requiring any a *a priori* knowledge for the construction of a suitable discretisation [22]. The application of adaptivity in problems of elasticity and thermoelasticity has been studied in [23, 24]. Adaptive isogeometric contact with polynomial splines over hierarchical T-meshes (PHT), has been explored in [25]. In [26] an adaptive hybrid isogeometric-meshfree collocation method for 2D contact problems has been investigated.

In the present study, we propose an adaptive isogeometric solver for frictionless contact problems, based on THB-Splines. The latter allow for a more efficient distribution of new degrees of freedom, thus reducing the problem size and computational cost significantly. First, we study the influence of the penalty constant on the conditioning of the system and demonstrate the superiority of NURTHS (Non-Uniform Rational Truncated Hierachical B-Splines), over *ad hoc* refined tensor product splines for the Hertz benchmark. Secondly, the aforementioned methodology is applied to the modelling of a pair of mating gear teeth. The generation of the boundary fitted tooth's geometry is performed by least squares fitting with B-Spline patches. Within this framework, investigations are performed with respect to the refinement indicators and strategies that drive the local adaptivity. In particular, we show that effective adaptive local refinement for gear contact problems can be achieved by using the vonMises stress as a marking indicator instead of costly *a posteriori* error estimators. A comparison against marking based on the strain energy density gradient shows that both approaches produce equivalent results. The performance of the proposed method is assessed with respect to fully refined meshes, to determine its accuracy compared to *ad hoc* refined tensor product patches to demonstrate the potential in efficiency and problem size reduction. To the best of our knowledge, this is the first time that a fully adaptive isogeometric contact modelling scheme, based on THB-Splines, is presented and applied to the simulation of gear contact problems.

The rest of the article is structured as follows. In Section 2 we present the contact formulation used, then Section 3 provides a brief overview of the theory of THB-Splines, their rational counterpart as well as adaptive mesh refinement strategies and markers. In Section 4 we develop standard benchmarks to verify our implementation and we perform a conditionning analysis for the Hertz benchmark, solved with NURTHS. In 5 the generation of the tooth geometry starting from design parameters is tackled by means of least squares B-Spline fitting, and the quality of the resulting spline models is assessed for different polynomial degrees. The gear contact simulation is showcased in Section 6, including a comparison of marking indicators and strategies that drive adaptive mesh refinement, resulting pressure profile curves and assessment of problem size versus obtained accuracy. In the last section the results are summarised and conclusions are drawn.

2. Contact formulation

Isogeometric analysis of contact problems has been very thoroughly summarised by de Lorenzis et al [13]. The authors group the available formulations into three families: (a) Collocation Methods, (b) Gauss Point to Surface (GPTS) methods and (c) Mortar methods.

Collocation methods are similar in spirit to the Node to Surface (NTS) [27] formulation from FEM. Node to surface (or segment) was a step forward from node to node algorithms and enabled the use of non-matching meshes at the contact interface. In NTS contact, the contact interface is regarded as a set of contact segments, and pressure is assumed to be constant within each segment. Penetration is then calculated as the average gap within each segment and constraints are enforced on it. Isogeometric analysis

naturally lends itself for use with collocation methods, since high polynomial orders and controllable continuity enable the direct enforcement of the contact constraints at the collocation points [28]. The major difference with respect to FEM, is that since the spline basis is not interpolatory, the constraints cannot be enforced at the control points themselves. Instead, some set of points that lie on the surface and are in one to one correspondence with the control points, must be used. As discussed in [29], Greville and Botella points are good candidates for the collocation of the contact integrals, with Greville points yielding marginally more accurate results. However, these methods fail to pass the contact patch test [30], and are sensitive with respect to the discretisation used and the choice of the, so called, master and worker side.

The GPTS approach aims to directly integrate the contact contribution to the weak form on the Gauss points defined on the worker contact surface. This makes it relatively simple to implement, once a suitable Gauss point projection method from worker to master is available. It has been shown to recover adequate results, even though some oscillations in the contact pressure have been observed due to the overconstrained nature of the formulation [31, 32].

Details of the isogeometric mortar method have been presented in [31, 32]. In contrast to the GPTS approach, the pressure is not defined locally, it is rather expressed as any other degree of freedom, on the basis itself. Thus a "control pressure" is assigned to every control point of the interface and is calculated based on the average control point penetration. Due to the non-interpolatory nature of the basis, "control pressures" do not have a physical meaning. The mortar approach revpromises increased accuracy, robustness and decrease of oscillatory behaviour, although it comes at the expense of increased complexity of implementation.

For the purposes of this study, the GPTS approach was selected as it offers a good trade-off between simplicity of implementation and performance. Contact will be considered frictionless, since for low friction coefficients, in particular less than 0.4, the effects of friction on the contact pressure distribution are negligible, see also [33]. As a result, the computational burden associated to the incorporation of the frictional evolution equations, is prevented.

The basic aspects of the formulation are presented in the sequel for the two dimensional, non-frictional setting. We consider two planar patches represented as splines

$$\mathbf{x}^{(m)}(u) = \sum_{i=1}^{Q^{(m)}} \mathbf{q}_i^{(m)} \beta_i^{(m)}(u) \quad , \quad m = 1, 2 \ , \tag{1}$$

where $\mathbf{q}^{(m)} \in \mathbb{R}^2$ are the control points, $Q^{(m)}$ is the number of control points and $\beta_i^{(m)}$ are the spline basis functions for the representation of body m.

2.1. Gap function and constraints

The first component of any contact formulation is the definition of the gap (or penetration) function. A distinction is made between the two bodies, one is assigned the role of "master" and the other that of the "worker". The selection is left to the user, but there are some guidelines in engineering practice, e.g. if a body is considerably stiffer that the other, it should be assigned the role of the master . For an arbitrary point on the worker surface, with position vector $\mathbf{x}^{(1)}(u)$, corresponding to parameter u, the gap function is defined as the difference between $\mathbf{x}^{(1)}(u)$ and its closest neighbour on the master surface $\mathbf{x}^{(2)}(v^*)$, with parameter v^*:

$$\mathbf{g}(u) = \mathbf{x}^{(1)}(u) - \mathbf{x}^{(2)}(v^*). \tag{2}$$

A closest point projection has to be preformed from the worker to the master to compute $\mathbf{x}^{(2)}(v^*)$. For a fixed parameter point u. the parametric coordinate v^* of the projected point on the master surface, is determined by minimising the squared distance function $\left(\mathbf{x}^{(1)}(u) - \mathbf{x}^{(2)}(v)\right)^2$ which leads to computing

the solution of

$$\left(\mathbf{x}^{(2)}(v) - \mathbf{x}^{(1)}(u)\right) \cdot \frac{d\mathbf{x}^{(2)}}{dv} = 0$$

with respect to $v \in \mathbb{R}^2$. Since the spline basis provides smooth and continuous normal and tangent vector fields, this task is well-defined, contrarily to FEM, where the kinks between adjacent elements pose a challenge. In our implementation a Newton iterative scheme has been used to solve this extremal condition.

Then the normal, or signed gap, is defined as the dot product of $\mathbf{g}$ with the normal vector $\mathbf{n}^{(2)}(v^*)$ of the master surface at the closest projection point :

$$g_N(u) = \mathbf{g}(u) \cdot \mathbf{n}^{(2)}(v^*). \tag{3}$$

This takes positive values where the bodies are separated and negative values in the regions where penetration occurs. Thus, since in contact modelling the two bodies must be separated or at most, barely touching each other, the normal gap needs to be greater or equal to zero, hence the so called non-penetration condition $g_N \geq 0$.

Another constraint that has to be met, is that the contact pressure exerted from one body to the other, has to be greater or equal to zero $p \geq 0$, i.e. the bodies cannot adhere to one another. Lastly, these two constraints are complementary in the sense that when the gap is zero, the contact force is positive and vice versa. This is expressed as $g_N \cdot p = 0$. Together these three conditions are known as the Karush-Kuhn-Tucker (KKT) conditions [34].

2.2. Constraint enforcement

There are multiple ways to incorporate the constraints in the problem formulation. The most commonly used methods are the Lagrange multipliers, Penalty and the Augmented Lagrangian method. The Lagrange method implies the introduction of more system variables, and thus the increase of the problem size and complexity, but satisfies the constraints exactly. Penalty methods on the other hand, do not increase the size of the system matrix, but only satisfy the constraints approximately, depending on the selection of the penalty parameter.

The augmented Lagrangian method aims to solve the shortcomings of the previous two methods. It does not introduce any new variables in the system and also is not dependent on the choice of penalty parameter. Instead two augmented Lagrangian multipliers are introduced, which by an iterative procedure, converge to the exact solution [35]. The obvious shortcoming of this method is that it requires the iterative solution loop of our non linear problem, to be nested within an augmentation loop, which increases the times that the system needs to be solved. For the scope of this work, the penalty method was selected due to its simplicity of implementation and efficiency.

Thus, the system's total potential is enriched with a new contact penalty term:

$$\Pi = \Pi_{\text{strain}} + \Pi_{\text{external}} + \Pi_{\text{contact}} \ , \tag{4}$$

where Π_{strain} is the body's potential energy due to its deformation and Π_{external} accounts for the work exerted from external loads. In the present work, we are restricted to small deformations and since gears are predominantly manufactured from some steel alloy, linear elastic material behaviour is assumed.

Since the penalty method is used to enforce the KKT constraints, this new term is taken as:

$$\Pi_{\text{contact}} = \frac{1}{2} \int_{\gamma} \epsilon \langle -g_N \rangle_+^2 \mathrm{d}\gamma \ , \tag{5}$$

where the bracket denotes the positive part of $-g_N$, γ is the contact interface and ϵ is the penalty parameter, which is chosen to have a sufficiently large value. Taking the variation of this potential, we get:

$$\delta\Pi_{\text{contact}} = \int_c \epsilon g_N \delta g_N \, \mathrm{d}c = \int_c \epsilon [\mathbf{x}^{(1)} - \mathbf{x}^{(2)}] \cdot (\delta\mathbf{x}^{(1)} - \delta\mathbf{x}^{(2)}) \, \mathrm{d}c \ , \tag{6}$$

where c is the part of the contact interface γ where penetration between the two bodies occurs.

2.3. Gauss Point to Surface

To evaluate this integral, the Gauss Point to Surface method suggests to numerically integrate it by means of Gauss quadrature on the worker surface, taking into account only the set of integration points $G^{(1)}$ which are in penetration with the master body, while neglecting the rest. Then the integral is approximated by the sum:

$$\delta\Pi_{\text{contact}} \approx \sum_{k\in G^{(1)}} \epsilon w_k J^{(1)}(u_k)\ [\mathbf{x}^{(1)}(u_k) - \mathbf{x}^{(2)}(v_k^*)] \cdot \left[\sum_{i=1}^{Q^{(1)}} \beta_i^{(1)}(u_k)\delta\mathbf{q}_i^{(1)} - \sum_{j=1}^{Q^{(2)}} \beta_j^{(2)}(v_k^*)\delta\mathbf{q}_j^{(2)}\right] , \quad (7)$$

where $\mathbf{q}^{(m)}$ are the control points, $Q^{(m)}$ is the number of control points and $N^{(m)}$ are the basis functions of body m, while w_k is the weight associated with quadrature point $k \in G^{(1)}$ and $J^{(1)}(u_k)$ is the norm of the tangent vector to the surface at the quadrature point k. Rearranging the terms we get

$$\delta\Pi_{\text{contact}} = -\sum_{i=1}^{Q^{(1)}} \mathbf{R}_i^{(1)}\delta\mathbf{q}_i^{(1)} - \sum_{j=1}^{Q^{(2)}} \mathbf{R}_j^{(2)}\delta\mathbf{q}_j^{(2)} , \quad (8)$$

where $\mathbf{R}^{(1)}, \mathbf{R}^{(2)}$ are the contact residuals for each body:

$$\begin{aligned} \mathbf{R}_i^{(1)} &= -\sum_{k\in G^{(1)}} \epsilon w_k J^{(1)}(u_k)\beta_i^{(1)} \left[\mathbf{x}^{(1)}(u_k) - \mathbf{x}^{(2)}(v_k^*)\right] \\ \mathbf{R}_j^{(2)} &= \sum_{k\in G^{(1)}} \epsilon w_k J^{(1)}(u_k)\beta_j^{(2)} \left[\mathbf{x}^{(1)}(u_k) - \mathbf{x}^{(2)}(v_k^*)\right] . \end{aligned} \quad (9)$$

By taking the derivatives of the residuals with respect to the control variables, the contact's contribution $K_{contact}$ to the system's tangent stiffness matrix can be calculated, for the system to be solved iteratively with the use of the Newton method.

$$K_{contact} = \begin{bmatrix} K^{(11)} & K^{(12)} \\ K^{(21)} & K^{(22)} \end{bmatrix}, \text{ where: } K_{ij}^{(mn)} = -\frac{\partial \mathbf{R}_i^{(m)}}{\partial \mathbf{q}_j^{(n)}} . \quad (10)$$

More details of this procedure can be found in [36].

As has been presented above, the standard GPTS formulation evaluates the contact integrals only on the worker side of the interface. This induces an inherent bias between master and worker surface. In order to mitigate this effect two alternative formulations have been proposed, that offer a symmetric treatment of both bodies.

2.4. GPTS-two-pass

This method splits the integral in two identical parts, where the role of master and worker is switched for each integral. Thus two summation passes have to be performed, over the Gauss points of two surfaces, hence the name of the 'two-pass' variant.

$$\delta\Pi_{\text{contact}} \approx \frac{1}{2}\int_{c^{(1)}} \epsilon \left[\delta\mathbf{x}^{(\mathbf{1})} - \delta\mathbf{x}^{(\mathbf{2})}\right] \cdot \left[\mathbf{x}^{(\mathbf{1})} - \mathbf{x}^{(\mathbf{2})}\right] \mathrm{d}c^{(1)} + \frac{1}{2}\int_{c^{(2)}} \epsilon \left[\delta\mathbf{x}^{(\mathbf{2})} - \delta\mathbf{x}^{(\mathbf{2})}\right] \cdot \left[\mathbf{x}^{(\mathbf{2})} - \mathbf{x}^{(\mathbf{1})}\right] \mathrm{d}c^{(2)}. \quad (11)$$

2.5. GPTS-two-field

The two-field method, like the previous one, splits the integral in two and switches the role of master and worker for each integral. This time only the basis functions associated to the current integration side are evaluated in each integral. This can be thought of as having two independent pressure fields, one for each body and equilibrium between the two is achieved in a weak sense.

$$\delta\Pi_{\text{contact}} \approx \int_{c^{(1)}} \epsilon\ \delta\mathbf{x}^{(\mathbf{1})} \cdot \left[\mathbf{x}^{(\mathbf{1})} - \mathbf{x}^{(\mathbf{2})}\right] \mathrm{d}c^{(1)} + \int_{c^{(2)}} \epsilon\ \delta\mathbf{x}^{(\mathbf{2})} \cdot \left[\mathbf{x}^{(\mathbf{2})} - \mathbf{x}^{(\mathbf{1})}\right] \mathrm{d}c^{(2)} . \quad (12)$$

3. Adaptive mesh refinement

Many problems which exhibit highly localised phenomena or singularities, and contact modelling is a prominent example of such a problem. In order to efficiently model these, a local refinement of the discretisation mesh is necessary [22]. In the isogeometric setting, classical B-Spline and NURBS parametrisations do not allow for local refinement due to their tensor-product structure. Thus more advanced, locally refinable spline constructions are necessary.

Since its introduction, many existing or novel technologies of locally refinable splines, have been applied to isogeometric analysis. Some of the most prominent are (truncated) hierarchical B-Splines (HB-/THB-)[37], T-Splines [21], locally refined (LR-)Splines [38] and polynomial splines over hierarchical T-meshes (PHT-)Splines [39]. For the scope of this work, THB-Splines were the construction of choice, since they possess all the desirable properties of tensor product splines, namely nonnegativity, partition of unity, smoothness and linear independence while still being relatively easy to implement and extend to higher dimensions. Their rational counterpart NURTHS is also available for problems where exact conic sections are involved, such as the Hertz benchmark problem. Furthermore, they preserve some of the underlying tensor product structure which can be exploited for the sake of computational efficiency. In the rest of this section the fundamentals of the construction of THB-Splines are presented. Then we present the general adaptive mesh refinement process and discuss different marking strategies for the discretisation of gear contact models.

3.1. Truncated Hierarchical B-Splines

We consider a finite sequence of nested bivariate (tensor-product) B–spline function spaces

$$V^0 \subset V^1 \subset \ldots \subset V^{N-1} \tag{13}$$

defined on the domain Ω^0. Let $\mathcal{B}^\ell$ be the tensor-product B–spline basis of the space V^ℓ of degree $\mathbf{p}^\ell = (p_1^\ell, p_2^\ell)$ and defined by knot sequences $T_i^\ell = (t_{i,j}^\ell)_{j=0}^{n^\ell}$, for $i = 1, 2$ and $\ell = 0, \ldots, N-1$.

We also consider a sequence of nested domains

$$\Omega^0 \supseteq \Omega^1 \supseteq \ldots \supseteq \Omega^{N-1}, \tag{14}$$

where each $\Omega^\ell \in \mathbb{R}^d$ represents a certain collection of cells with respect to the tensor-product grid of refinement level ℓ.

The multivariate hierarchical model allows to consider different kinds of refinement, degrees, and smoothness as long as the nested nature of the spline spaces (13) is preserved. For the sake of the presentation, and without loss of generality, we restrict ourselves to dyadic cell refinement with equal component degrees $\mathbf{p}^\ell = (p, p)$ at each refinement level ℓ.

We denote by $\operatorname{supp} f$ the support of a function f, that is, the domain where the value of f is non-zero. The following definition allows to construct a basis for the hierarchical B–spline (HB) space [40].

The hierarchical B–spline basis $\mathcal{H}$ is constructed as follows.

(I) Initialisation: $\mathcal{H}^0 = \left\{ \beta \in \mathcal{B}^0 : \operatorname{supp} \beta \neq \emptyset \right\}$.

(II) Recursive construction: $\mathcal{H}^{\ell+1} = \mathcal{H}_A^{\ell+1} \cup \mathcal{H}_B^{\ell+1}$, for $\ell = 0, \ldots, N-2$, where

$$\mathcal{H}_A^{\ell+1} = \left\{ \beta \in \mathcal{H}^\ell : \operatorname{supp} \beta \not\subseteq \Omega^{\ell+1} \right\}, \; \mathcal{H}_B^{\ell+1} = \left\{ \beta \in \mathcal{B}^{\ell+1} : \operatorname{supp} \beta \subseteq \Omega^{\ell+1} \right\}.$$

(III) Final basis: $\mathcal{H} = \mathcal{H}^{N-1}$.

HB-Splines are non-negative, linearly independent [40], and their span contains all piecewise polynomial functions defined on a certain class of suitable underlying hierarchical mesh [41, 42]. However, they do not form a partition of unity, since the sum of hierarchical B-Splines at different refinement level may be greater than one.

Let $\tau \in V^\ell$ and let

$$\tau = \sum_{\beta \in \mathcal{B}^{\ell+1}} c_\beta^{\ell+1}(\tau)\beta, \qquad c_\beta^{\ell+1} \in \mathbb{R}, \tag{15}$$

be its representation with respect to the finer basis of $V^{\ell+1}$. The truncation of τ with respect to $\mathcal{B}^{\ell+1}$ and $\Omega^{\ell+1}$ is defined as

$$\operatorname{trunc}^{\ell+1}\tau = \sum_{\beta \in \mathcal{B}^{\ell+1},\, \operatorname{supp}\beta \not\subseteq \Omega^{\ell+1}} c_\beta^{\ell+1}(\tau)\beta. \tag{16}$$

The following definition allows to construct a different set of basis functions, called truncated hierarchical B-Splines (THB-Splines) [37], which span the same spline space of HB-Splines.

The truncated hierarchical B–spline basis $\mathcal{T}$ is constructed as follows.

(I) Initialisation: $\mathcal{T}^0 = \mathcal{H}^0$.

(II) Recursive construction: $\mathcal{T}^{\ell+1} = \mathcal{T}_A^{\ell+1} \cup \mathcal{T}_B^{\ell+1}$, for $\ell = 0, \dots, N-2$, where

$$\mathcal{T}_A^{\ell+1} = \left\{ \operatorname{trunc}^{\ell+1}\tau : \tau \in \mathcal{T}^\ell \wedge \operatorname{supp}\tau \not\subseteq \Omega^{\ell+1} \right\}, \ \mathcal{T}_B^{\ell+1} = \mathcal{H}_B^{\ell+1}.$$

(III) Final basis: $\mathcal{T} = \mathcal{T}^{N-1}$.

The truncated basis $\mathcal{T}$ satisfies the partition of unity, and allows us to extend it seamlessly to NURTHS (Non-Uniform Rational Truncated Hierarchical B-Splines) basis functions by assigning scalar weights to each member of the basis, completely analogously to classical NURBS. If all weights are set equal to one, then the weight function is equal to one, thus we recover polynomial THB-Splines.

3.2. Iterative refinement with adaptivity

The process of selecting, or marking as it is more commonly called, the elements that will be further refined, can be a laborious task. It is not always straightforward to decide where the new degrees of freedom shall be allocated. More specifically in contact problems, it is not always the case that the actual contact point is known *a priori*. Thus, it is necessary to automate the refinement procedure with some adaptivity routine. The basic overview of an adaptively refined simulation workflow is presented in Figure 1. Starting with a coarse mesh, an initial simulation is performed, and then based on the results and some sort of refinement indicator, elements are marked and then further refined. Optionally, as in our case, the previous solution is projected to the refined spline space, in order to have a better initial estimate for the next solution. This loop is repeated until the convergence criteria for some quantity of interest are met, or a maximum refinement level is reached.

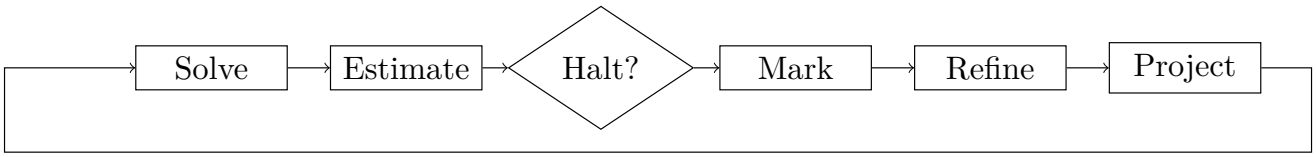

Figure 1: Adaptively refined simulation flow chart.

3.3. Refinement indicators

In order to adaptively refine the element mesh, the definition of some indicating quantity is necessary. Commonly some *a posteriori* error estimator is used in order to allocate degrees of freedom in areas where the error is greatest. These can be grouped into four main categories. First there are residual-based error estimators [43, 22] which have stronger mathematical foundations and their theoretical properties can be analytically derived. However these tend to be more complex to implement, especially in cases with complicated loads, such as contact. Then there are recovery-based and goal-oriented methods. The

former aim at constructing an approximation of the quantity of interest, by sampling and fitting the current solution on specially selected points [44, 45]. This yields an approximation of the exact quantity of interest which is better than what the current solution provides and thus an error estimate can be defined based on that. Goal-oriented methods commonly involve the solution of a dual problem on an enriched space for the definition of an error estimate [46, 47]. As it is apparent, extra computational overhead is introduced for both aforementioned methods.

A fourth option, which combines several advandages of the aforementioned ones [48], are the gradient-based indicators. They essentially encapsulate the engineering practice, which states that more degrees of freedom are needed to approximate areas which have higher gradient in some quality of interest. Their main advantage is that they introduce very little computational overhead, and they re easy to develop and implement. Despite not being as mathematically founded as residual-based methods, they perform really well, in particular for our contact problem, as we shall demonstrate in Section 6. In particular, we utilised the strain energy density as a refinement indicator, in similar spirit to [26].

The strain energy density for an isotropic linearly elastic body is given as:

$$W = \mu\ \varepsilon : \varepsilon + \frac{\lambda}{2}\ \mathrm{trace}(\varepsilon)^2\ , \tag{17}$$

where ε is the strain tensor and μ, λ are Lame's material parameters. Then, the components of its gradient are as follows:

$$\frac{\partial W}{\partial x_c} = 2\mu\ \varepsilon : \frac{\partial \varepsilon}{\partial x_c} + \lambda\ \mathrm{trace}(\epsilon) \cdot \mathrm{trace}\left(\frac{\partial \varepsilon}{\partial x_c}\right)\ , \tag{18}$$

where x_c denotes the coordinates of an arbitrary domain point $\mathbf{x}$.

The final approach that we have considered is to use the value of vonMises stress as a marking indicator. Indeed, for our specific gear problem we may intuitively consider that refinement should be concentrated in two areas: the root fillets, and the contact region. These are the areas that commonly exhibit the highest stress values, and for this reason the vonMises stress may be directly used as a marking indicator. This approach does not introduce additional computational cost, as stresses are standard quantities that are typically calculated in elasticity simulations. The vonMises stress for a two dimensional elastic medium is directly calculated from the components of the stress tensor, which is already computed, as:

$$\sigma_{\mathrm{vMises}} = \sqrt{\sigma_{xx}^2 + \sigma_{yy}^2 - \sigma_{xx}\sigma_{yy} + 3\tau_{xy}^2}\ . \tag{19}$$

The induced elementwise refinement indicators are therefore

$$I_K^{\mathrm{SED}} = \max_{\mathbf{x}\in K} \|\nabla W(\mathbf{x})\|_2 \quad \text{and} \quad I_K^{\mathrm{vM}} = \max_{\mathbf{x}\in K} \|\sigma_{\mathrm{vMises}}(\mathbf{x})\|_2$$

for each element K in the mesh.

The two aforementioned indicators are assessed experimentally in Section 6.3 for the gear contact problem. Our conclusion is that the stress-based indicator is as robust and efficient as the one based on strain energy density.

3.4. Marking strategy

As for the marking strategy, two different approaches are considered. The first variant marks a fixed percentage of the existing elements, where the indicator has its largest values. The second marks elements in decreasing indicator value, until a certain percentage of the sum of the indicator values of all elements is reached. This is also known as Dörfler marking [49], although this approach is more commonly used with error estimators. The adaptive refinement loop is halted, either when a quantity of interest (e.g. the maximum pressure) has converged to a value, or a maximum refinement level has been reached.

Note that, regardless of the marking strategy used, if a part is represented by a collection of adjacent C^0–conforming patches, the refinement is propagated to the coarser side, to avoid T-junctions on the interface and thus maintain C^0–conformity.

4. Validation

To ensure the validity of the implementation of the aforementioned methodologies, two classic contact benchmark problems are elaborated in this section. The first is the contact patch test, introduced in [30] and the second is the Hertzian contact problem in two dimensions.

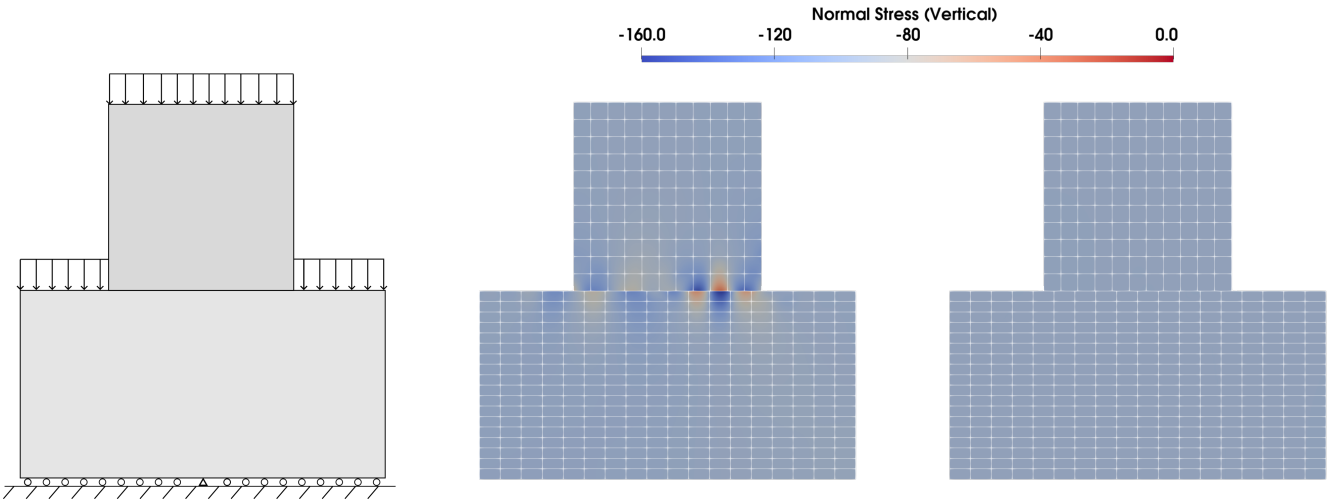

Figure 2: Patch test. From left to right: problem setup, GPTS-standard and GPTS-two-field vertical normal stress fields. Oscillations observed in GPTS-standard method are not present when GPTS-two-field is used.

4.1. Contact patch test

The patch test problem in two dimensions consists of two dissimilar rectangular patches, with the smaller of the two resting on top of the other. The bottom patch is fixed along its lower side, and a uniform downward ambient distributed load is applied on all the exposed upper horizontal surfaces of both patches. Both are modelled with bi-quadratic B-Spline patches, with a total of 1085 degrees of freedom. The expected outcome is to recover a uniform vertical normal stress field, equal to the applied traction of 100 N/mm in both patches.

All three formulations presented in Sections 2.3 - 2.5 have been applied to this setup, using B-Splines of second order with non-conforming elements and the results can be seen in Figure 2. The GPTS-standard and GPTS-two-pass methods fail deliver a uniform stress field and exhibit an oscillatory behaviour in the contact regions. This result is inline with previous studies [36], and is accredited to the bias between master and worker bodies as well as the dissimilarity of the interacting meshes which results into elements that are partially in contact. The third method, GPTS-two-field achieves an accurate and uniform stress field everywhere, and thus passes the contact patch test.

4.2. Hertzian contact benchmark

Hertzian theory provides analytical solutions for contact problems of small deformations, for bodies of constant curvature in two and three dimensions. For the purposes of this study, the contact between an infinite elastic cylinder of 10 mm radius and an elastic half-space, both with a Young's modulus of $E = 2.1 \cdot 10^5$ N/mm^2 is investigated. As both objects are infinitely long, a two-dimensional section was examined, under plane strain assumptions. Due to symmetry, only a quarter of the cylinder is modelled with the appropriate boundary conditions, as seen in Figure 3a. In addition, for the sake of avoiding a singular parametrization at the center of the cylinder, we cut away a circular section around that region. Therefore the cylinder is represented by a NURBS quarter-annulus of degree two (this allows for an exact replication of the circular arc at the contact interface). As shown in Figure 3b, a small region close to the contact point is uniformly refined on both parametric directions to an element size of $h_{\min} = 0.052$ mm.

The uniformly distributed load of $p = 100$ N/mm of the full cylinder is modified as $p_i = p\cos\phi$ to take into account the missing circular section, cf. [31].

A second model was constructed, starting from the coarsest NURBS discretisation, with *a priori* refined NURTHS. The elements of the sixth level of uniform refinement, that are within a small rectangular region close to the theoretical contact point, were inserted in the THB-Spline mesh. For obtaining comparable discretisations, the elements in the refined region have exactly the same size of $h_{\min} = 0.052$ mm and the two meshes are locally identical. In order to obtain a valid hierarchical mesh, the refinement propagates to neighbouring elements from the intermediate hierarchical levels and consequently a gentle transition from coarse to fine elements is achieved, as seen in Figure 3c. The final THB-Spline model preserves the exactness of the circular geometry, thanks to the use of rational functions.

The resulting pressure distributions, normalised by the theoretical pressure $p_0 = 2701.54\,\mathrm{N/mm^2}$ and half-width $a = 0.471\,\mathrm{mm}$, for the refined bases are presented in Figure 4a. We observe that the GPTS-two-field approach yields results that are in very close agreement to the analytical solution, both in terms of maximum pressure, as well as in terms of contact area width. An oscillatory behaviour appears near the edge of the contact area. This effect is in accordance with the findings of previous studies, cf. [31, 32], and stems from the fact that a continuous and smooth basis is used to approximate something inherently discontinuous. These oscillations decrease significantly in magnitude when further refining the region, and they are not a matter of major concern for the our study since the contact pressure and width are predicted accurately. Furthermore, the NURTHS produce almost identical results to the uniformly refined NURBS with a generous reduction of 41% in the total number of degrees of freedom.

4.3. Conditioning of the Hertz benchmark

Contact problems are numerically very challenging and especially in combination with the penalty method, the resulting system of equations may not be numerically robust. In this class of constraint enforcement methods, the selection of the penalty constant ϵ is an important choice that is made manually by the user. Increasing the penalty parameter ϵ leads to worse conditioned systems, but decreases the inherent unphysical penetrations, thus improving the accuracy [19, 31, 32]. Another factor impacting the conditioning is the discretization basis; in this regard, THB-Splines are known to have reasonably good conditioning for Galerkin discretisations of PDEs [50]. To investigate these phenomena, we perform a study of the condition number of the involved matrices with respect to the penalty parameter and the error in maximum pressure for the two discretisations presented in the previous section.

The results are presented in Figure 4b. We observe that, on the one hand, increasing ϵ does indeed decrease the error but leads to badly conditioned systems and ultimately to unsolvable systems, which were omitted from the diagram. On the other hand, decreasing the constant relaxes the enforcement of the constraints and naturally the system becomes easier to solve but larger penetrations are allowed and the accuracy of the solution is severely hindered.

It is interesting to see that by using the rational THB-Spline basis for discretisation, a sharp decrease in the condition number of the system is observed, by one to two orders of magnitude, depending on ϵ. The propagation of the refinement across the entire parametric domain, due to the inherent tensor product structure of NURBS, creates slender elements of very high aspect ratio which inhibit the conditinoning of the system. One could expect the hierarchical mesh to have higher condition numbers, considering the fact that the ratio of the largest to smallest element size, is larger in this case, namely $\frac{h_{\max}}{h_{\min}} = 69.42$ for NURTHS and 32.05 for NURBS. However, this is not the case, owning to the fact that the NURTHS elements have a more consistent aspect ratio, and are transitioning smoothly from coarse to fine elements, achieving a condition number of one order of magnitude lower than NURBS.

Regarding the selection of the penalty constant ϵ, considering the findings of our numerical experiments, the value of $\epsilon = 100 \cdot E$ was retained, where E is the material elasticity modulus, since it achieves a small-enough deviation from the analytical pressure value of approximately $4{\cdot}10^{-3}$, while still having a reasonable condition number. This penalty value will be used for all of the following simulations, unless otherwise specified.

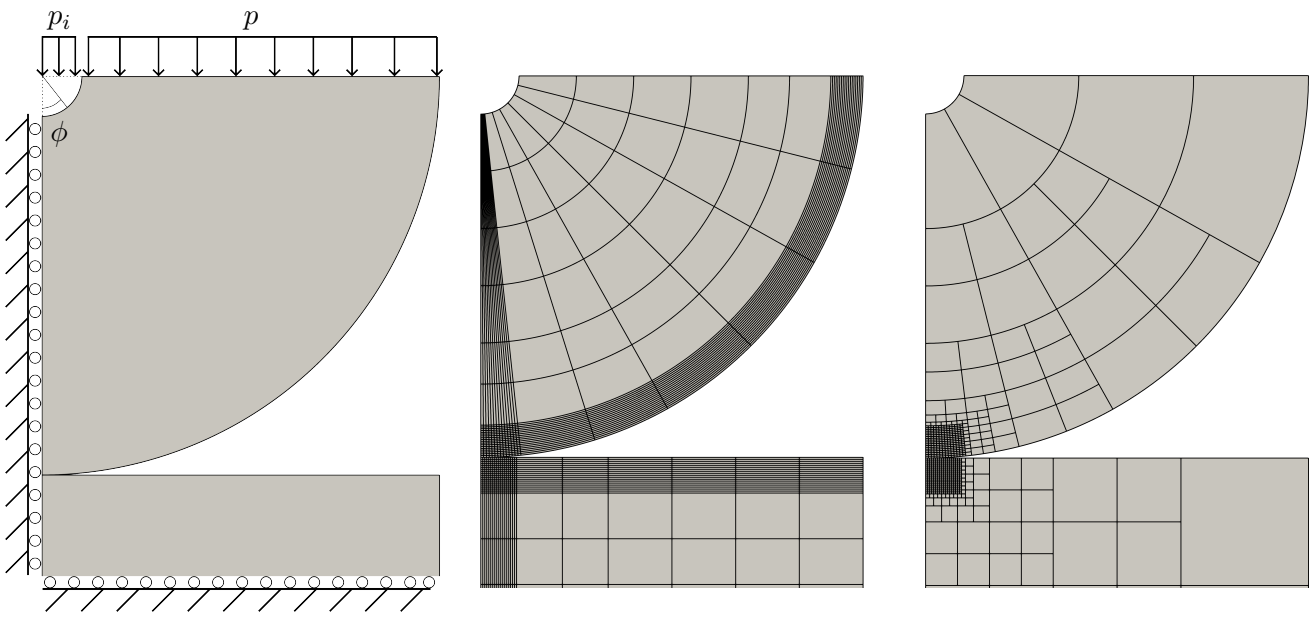

(a) Geometry and boundary conditions. (b) NURBS. 2418 DOF, $h_{\min} = 0.052$ mm (c) NURTHS. 1425 DOF, $h_{\min} = 0.052$ mm

Figure 3: Hertz benchmark, (a) problem setup, (b) NURBS discretisation, (c) NURTHS discretisation.

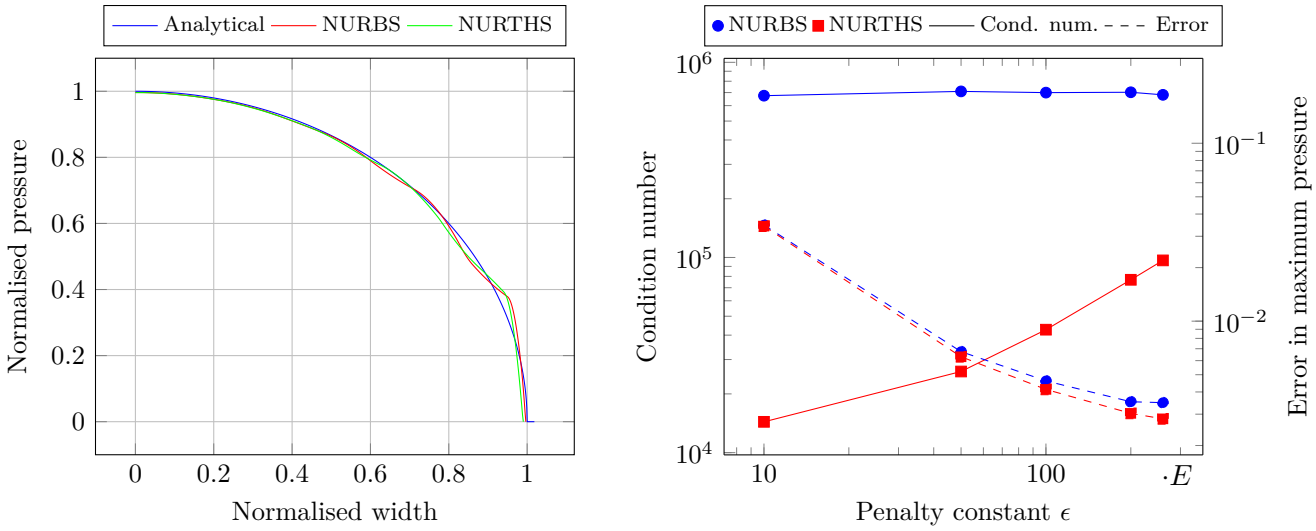

(a) Pressure distributions, for $\epsilon = 100 \cdot E$.

(b) Condition number study of Hertz benchmark.

Figure 4: Results of Hertz benchmark. (a) Pressure distributions for all discretisations. (b) Conditioning study for varying penalty constants. NURTHS are favorable with respect to condition number while offering the same level of accuracy as NURBS.

5. Gear geometry generation

A boundary fitted geometric representation of the gear teeth geometry is necessary to perform our isogeometric simulation. In this section we generate the gear geometry using few Bézier patches.

The most commonly used tooth profile is the involute [51]. Despite its widespread use, the geometry of an involute spur gear is very intricate. Its flank is composed of two regions: a portion of a circle's involute and the root fillet. The theoretical manufacturing of a gear with a rack is depicted in Figure 5. Given the gear's module m, pressure angle α, number of teeth z, and profile shift coefficient x , the equation of the

involute part, parametrised by the roll angle ϕ is [52]:

$$\begin{aligned} x(\phi) &= -r_b(\sin(\phi+s) - \phi\cos(\phi+s)) \\ y(\phi) &= \ \ r_b(\cos(\phi+s) + \phi\sin(\phi+s)) \ , \end{aligned} \tag{20}$$

with $s = -\tan\alpha + \alpha - \dfrac{\pi}{2z} - \dfrac{x\sin\alpha}{r_b}$ and base circle radius $r_b = \dfrac{mz}{2}\cos\alpha$. The shift angle s is introduced so that the resulting tooth is centered on the vertical axis, taking the profile shift into account.

The equation for the tooth root fillet which is part of a trochoid curve, parametrised by the angle θ between the coordinate system attached to the gear tooth and that which is attached to the generating rack, is given by [53]:

$$\begin{aligned} X_F(\theta) &= Y_{C0}\cdot\sin\theta + (X_{C0} - r\theta)\cdot\cos\theta - r_T\cdot\sin\gamma \\ Y_F(\theta) &= Y_{C0}\cdot\sec\theta + (r\theta - Y_{C0}\cdot\tan\theta - X_{C0})\cdot\sin\theta - r_T\cdot\cos\gamma \ , \end{aligned} \tag{21}$$

with:

$$\begin{aligned} X_{C0} &= [h_A + r_T(\sin\alpha - 1)]\cdot\tan\alpha + r_T\cdot\cos\alpha + \frac{m\pi}{4} \\ Y_{C0} &= r + r_T + x - h_a \\ \gamma &= \tan^{-1}\left(\frac{r\theta - X_{C0}}{r - Y_{C0}}\right) + \theta \ , \end{aligned}$$

where $r = \dfrac{mz}{2}$ is the gear's reference circle radius, r_T is the cutting rack's root radius and h_a is the rack's addendum coefficient.

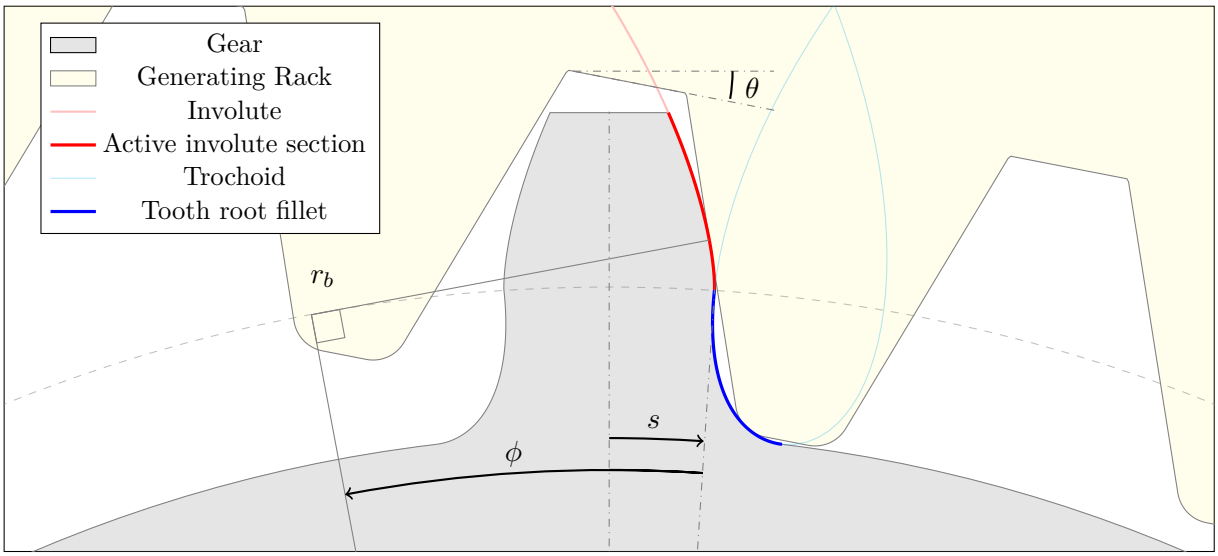

Figure 5: Schematic of gear's construction. The generating rack removes material from the gear blank as it is translated tangentially with a constant rate to the blanks's rotation. The involute curve (red) is parametrised by roll angle ϕ, offset angle s and base circle radius r_b while the trochoid curve (blue) by angle θ.

Since both the involute and the trochoid curves are transcendental, they cannot be exactly represented neither as an algebraic or rational curve, nor as a NURBS parametric curve. Thus, a fitting procedure has to be developed in order to come up with an accurate approximation of the analytical curves. We will use polynomial B-Splines for this task, since fitting with NURBS is more complicated while the accuracy gains are marginal, with the exception of conic sections [54]. Furthermore, the cost of evaluating NURBS basis functions and their derivatives is higher, thus negatively impacting the time required for assembly

of each iteration's tangential stiffness matrix for no good reason. The parameter range for both ϕ and θ is determined by solving the intersection of the two curves numerically, as well as the intersections of the involute with the gear's tip circle and between the fillet and the root circle.

Two different approaches were tested for the approximation of the involute curve. This is the area where contact between the gears occurs, and thus geometric accuracy is most important. The first approach was sampling of the curve and a least squares fitting of a Bézier curve on the point cloud. The second approach was the method described by Higuchi et al. [52]. It involves the use of Chebyshev polynomials to approximate the curve and a subsequent conversion to the Bernstein basis.

The maximum and root mean square errors of the fitting procedure for various degrees of Bézier curves are presented in Table 1, normalised by the pitch diameter. A least squares fitting with degree four Bézier curves is chosen in the current study, since its accuracy is very close to that of the respective result from the Higuchi method. Moreover with the least squares approach, one can impose restrictions to ensure that the endpoints of the Bézier curve lie on the exact involute curve, which applies to our implementation. This method is also more flexible since it is not restricted to the use of the Bernstein basis.

	Least Squares		Higuchi et al.	
	Max. error	RMS error	Max. error	RMS error
$p = 2$	$1.50113 \cdot 10^{-4}$	$1.11165 \cdot 10^{-4}$	$2.54899 \cdot 10^{-3}$	$1.76894 \cdot 10^{-3}$
$p = 3$	$4.68609 \cdot 10^{-5}$	$2.67343 \cdot 10^{-5}$	$2.20588 \cdot 10^{-4}$	$4.10642 \cdot 10^{-5}$
$p = 4$	$2.02077 \cdot 10^{-5}$	$9.68141 \cdot 10^{-6}$	$1.33458 \cdot 10^{-5}$	$9.14763 \cdot 10^{-6}$

Table 1: Maximum error and root mean square error for the fitting of the involute using Bezier curves by means of least squares (left) or Chebyshev polynomials [52] (right).

From the resulting curve, a surface is generated by mirroring it along the tooth's symmetry axis and then introducing a third column of control points, so that the inner and outer most edges of the patch, are circular arcs. The pair of patches that is used for the experiments of Section 6, representing the pinion and the gear, along with their control points and knot vectors can be found in Appendix A. After the patches for both gears have been created, they must be positioned in a mating configuration. To do so, we first translate them according to the specified axial distance a and then rotate them accordingly, so that they contact each other at the pitch point. Then, by specifying an arbitrary distance along the line of contact between the desired contact point and the pitch point, the gears assume their final position.

6. Application, Results and discussion

The methodologies discussed, have been implemented within the framework of G+Smo (Geometry plus Simulation Modules) [55] and applied for the modelling of the FZG-A [56] gear pair, used in efficiency testing rigs. This specific set was selected because it is one of the most popular standardised gear sets. Its two gears have very dissimilar geometries, due to the profile shifts that have been used. The pinion has wide and almost pointed teeth whereas the gear exhibits undercutting. The engineering design parameters of the gear pair are presented in Table 2, whereas their degrees, knot vectors and control points are given in Appendix A.

	Gear	Pinion
Module m	4.5 mm	
Axial distance a	91.5 mm	
Number of teeth z	24	16
Profile shift coeff. x	-0.5	0.8532
Tip diameter	112.5 mm	88.77 mm

Table 2: FZG-A gear pair's design parameters.

6.1. Setup

The tooth pair is positioned so that contact occurs at the pitch point. Both bodies are considered linearly elastic with the same modulus of elasticity $E = 2.1 \cdot 10^5$ N/mm^2. The boundary conditions applied to the two patches are illustrated in Figure 6 and are the following: the pinion patch is fixed along its inner most edge, as well as its sides below the root circle. The gear patch has a Dirichlet boundary condition of a prescribed rotation $\mathrm{d}\theta = 10^{-4}$ radians around its center, applied to its respective sides. The flanks of the teeth where contact between the two bodies will occur, constitute an interface between the patches, which has been marked red. The contact residual and it's contribution to the tangential stiffness matrix, will be integrated on this interface.

This setup will serve as a common basis for all the numerical experiments that follow. In each of the following sections, one aspect of the problem is varied in order to assess its influence on the obtained results.

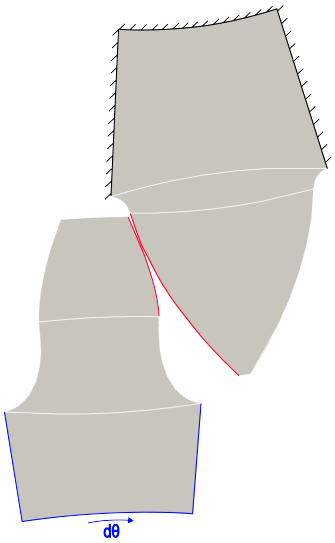

Figure 6: Boundary conditions: The pinion (right) is fixed along its inner most edge and the two adjacent sides. The gear (left) has a prescribed rotation around its center, applied to its circular base and the two lower sides. The edges of the two bodies where potential contact is possible depicted in red.

6.2. Comparison between tensor product and THB-Splines

The first experiment aims to verify the integrity of the results acquired with the THB-Spline basis, as well as to compare its performance against *a priori* refined tensor product meshes. Thus three models were compared, the first being a fully refined tensor B-Spline model of degree two, which serves as the reference solution. The second was an adaptively refined THB-Spline model, starting from the same initial discretisation. To drive the adaptivity routine, the strain energy gradient was used as a marking indicator and 20% of the elements were marked for refinement at each iteration. The last model is based again on the same coarse, degree two B-Spline mesh, but the elements close to the theoretical contact point from the kinematic of gears, were subdivided at each refinement step. The resulting pressure distributions for all three models are presented in Figure 7. The *ad hoc* refined tensor product and the THB-Spline meshes, that were obtained after three refinement iterations, can be seen in Figure 8.

As we can see on the overall pressure profile (Figure 7a), there is generally a good agreement between all three approaches. Focusing closer on the region of maximum pressure (Figure 7b), the three models start to part. The baseline fully refined tensor product model reports the lowest maximum pressure of 503.028 MPa. The THB-Spline model manages to closely match that pressure profile, with a maximum pressure of 503.177 MPa whereas the *a priori* refined tensor product diverges from the two, overshooting

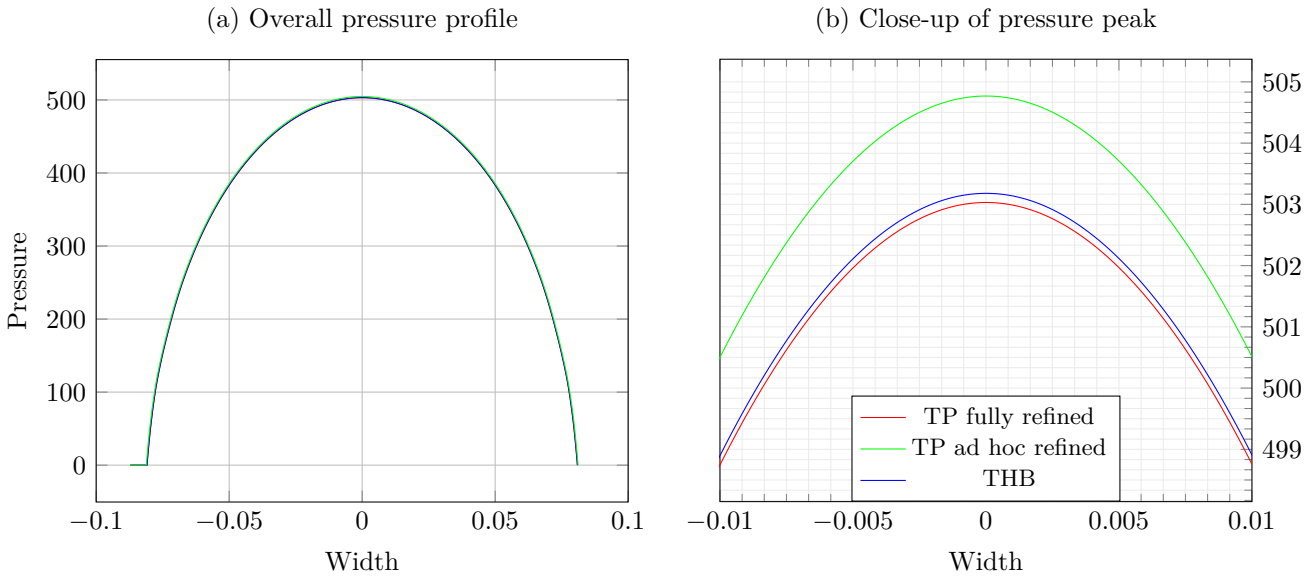

Figure 7: Comparison of contact pressure between second degree fully refined TP Spline (red), *ad hoc* refined TP spline (green) and THB-spline (blue).

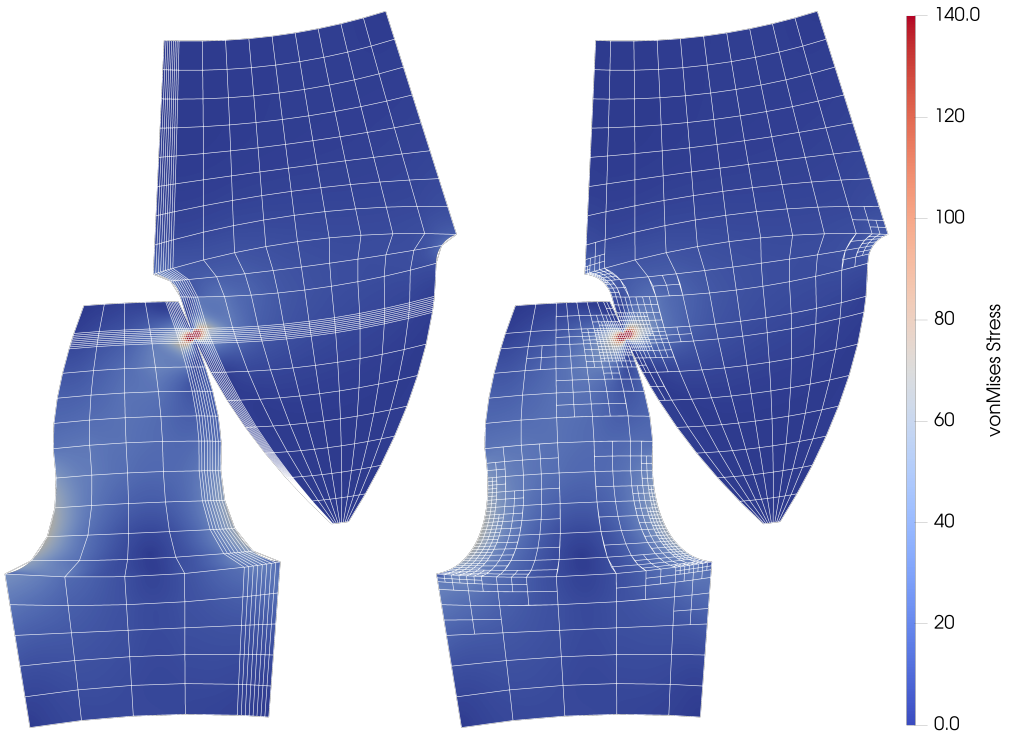

Figure 8: Comparison of *ad hoc* refined tensor product mesh (left) and THB mesh (right), both for 3 levels of adaptive refinement iterations.

the maximum pressure at 504.765MPa. The error is small, but it is in fact ten times higher than that of the THB-Spline model.

This effect can be explained by the differences between the two meshes, that can be observed in Figure 8. Locally, at the vicinity of the contact region, the elements of both models are identical, since they stem from the same original mesh and are produced by dyadic refinement. However, when we move far from the contact region, the two meshes are very different, since the *a priori* refined tensor product mesh

still has large elements in the bulk of the patch, whereas the THB model achieves a smoother transition from fine to coarse elements. Moreover, the two meshes differ vastly in terms of degrees of freedom. The fully refined mesh, after 7 refinement iterations, has 8,870,160 DOFs, the locally refined 80,490, whereas the THB refined mesh only has 14,860 DOFs.

6.3. Refinement indicators

The second test focuses on the selection of the refinement indicator. Two candidates are evaluated, the vonMises stress and the strain energy density gradient. The same setup is used once more, this time with the THB discretisation of quadratic degree and a fixed percentage marking strategy set to refine 20% of the elements at each iteration. Thus the number of degrees of freedom is almost identical at each refinement level for both models and after 7 refinement iterations it is around 14,000. Small deviations occur when elements that lie on the interface between adjacent C^0 patches are marked, because the marking is propagated to the other side as described in Section 3.4

Both indicators are in very good accordance, as seen in Figure 9. This means that for our particular case of study, even the simplest possible indicator quantity, manages to deliver as accurate results, as the relatively more complex gradient based indicator. Furthermore, the resulting meshes are very similar as can be seen in Figure 10 after 4 refinement loops and in Figure 11 for the vicinity of the contact region at the finest level. Nevertheless, the gradient based indicator is more generally applicable to a wider class of problems and loading scenarios [48]. Thus in all subsequent THB models we use this indicator, unless specifically mentioned otherwise.

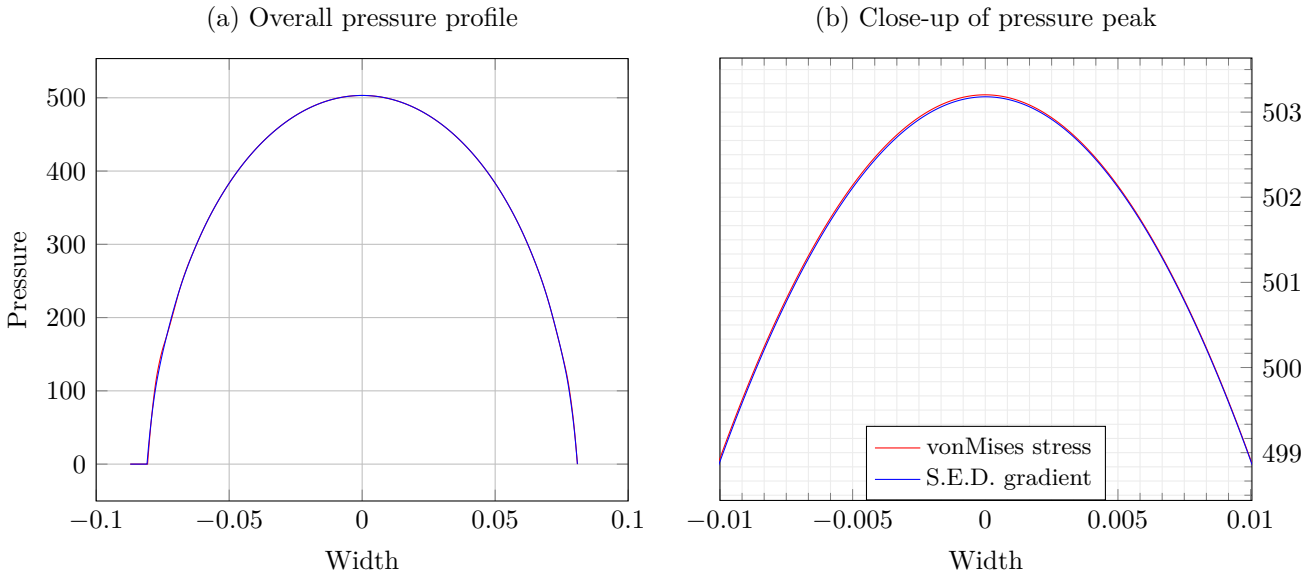

Figure 9: Comparison of indicators von Mises (red) vs Strain Energy Density gradient (blue).

6.4. Marking strategy

To investigate the effect of marking strategies, THB models constructed with the two different strategies outlined in Section 3.4 are compared, namely fixed percentage and Dörfler marking. Both models start from the same quadratic coarse tensor product spline, as in the previous section, and marking is performed based on the strain energy density gradient. The fixed percentage strategy was set up to refine 20% of the elements at each iteration, where as the refinement threshold for the Dörfler strategy was tuned to 5.6%, so that the two discretisations have comparable degrees of freedom. The resulting element meshes after 3 levels of refinement are depicted in Figure 13. The two meshes exhibit high ressemblance, with the differnce that the Dörfler strategy has allocated new degrees of freedom more sparingly.

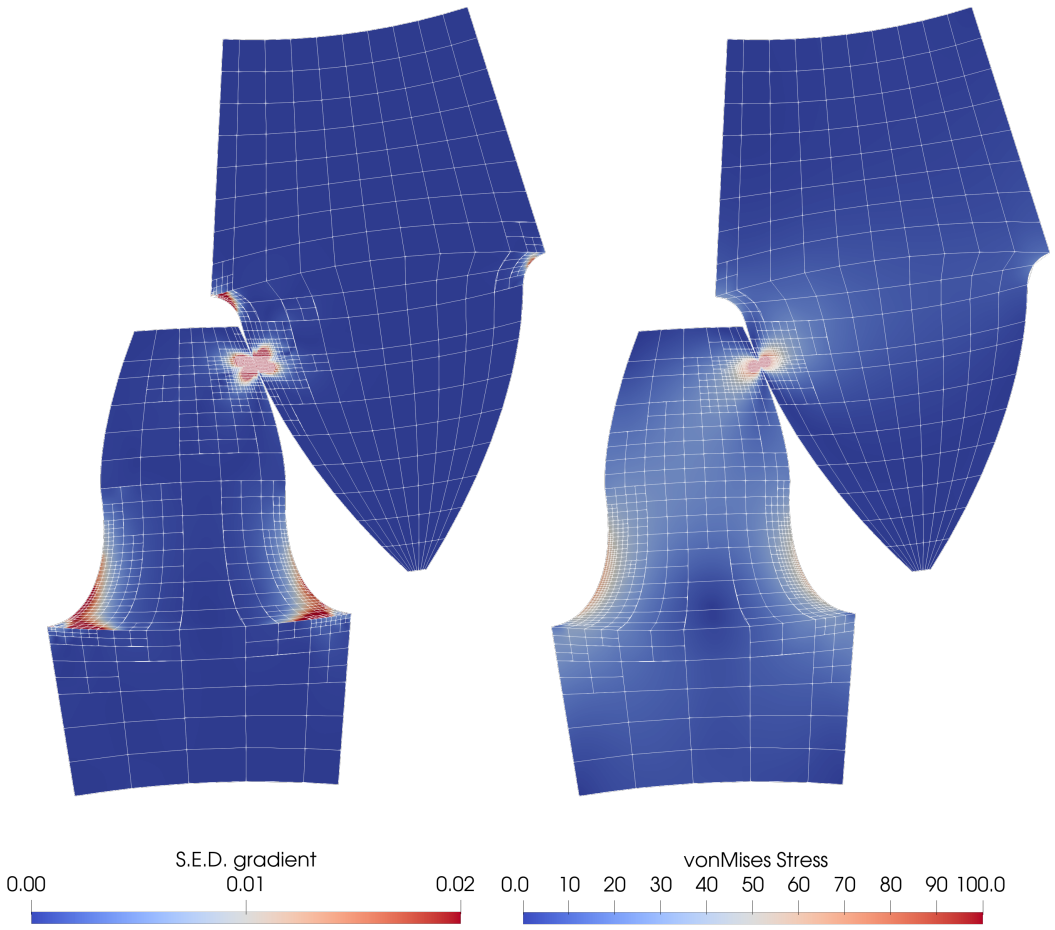

Figure 10: Comparison of THB meshes produced with different refinement indicators, strain energy density gradient (left) and vonMises stress (right), both for 4 levels of adaptive refinement iterations.

In Figure 12 the relative error with respect to the fully refined tensor product B-Spline solution is plotted against the degrees of freedom at each refinement step. The Dörfler strategy seems to distribute degrees of freedom more efficiently and achieves faster convergence. The fixed percentage strategy also performs well, but it requires more degrees of freedom to achieve the same accuracy as the Dörfler one. One benefit of fixed percentage is that the number of elements at each refinement step is known *a priori*, since the number of elements at each level has a fixed ratio to the previous one.

6.5. Polynomial degree

The last test examines the influence of the polynomial degree of the spline patches on the resulting pressure distribution. Since the geometry was constructed by fitting the involute with a Bézier curve of fourth degree, models with different degree were obtained by elevating or reducing the degree of that initial model. The experiment was conducted for fully and *ad hoc* refined tensor product splines as well as THB-Splines. The experiments of this section were performed using six levels of adaptive refinement. Looking at Figures 14 and 15, we can see that the overall pressure profiles for globally refined and THB-Splines are in good agreement for all degrees. One can observe that in both cases, the discretisations of degrees lower than four (the degree used to fit the involute) yield slightly lower maximum pressures, whereas the results for degrees 4 and 5 are very close. That might be due to the geometrical deviation that is introduced by lowering the degree, which impacts the solution, since it changes the geometry of the problem and in particular of the contact interface. This highlights the fact that geometrical accuracy is of utmost importance when modelling contact. An overview of the maximum pressure obtained for polynomial degrees from 2 to 5 for all types of discretisations is presented in the left part of Table 3.

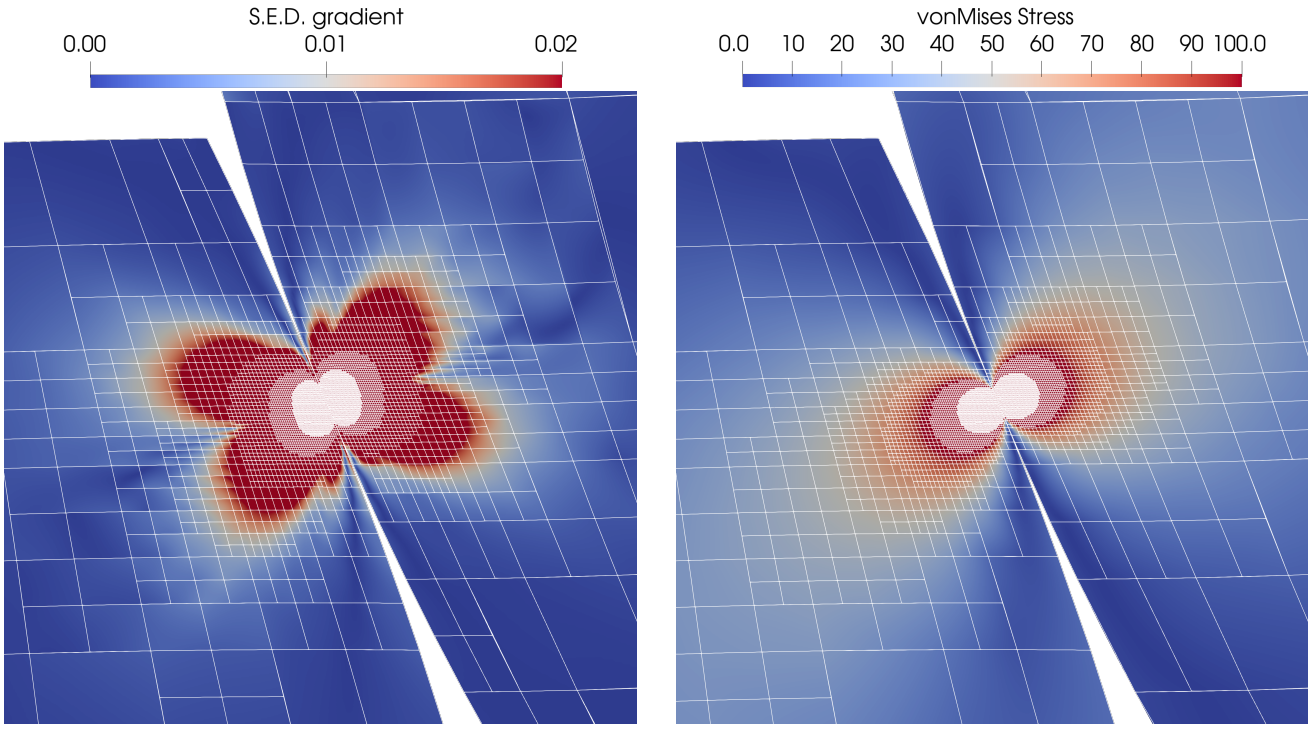

Figure 11: Close-up of adaptively refined THB meshes. Refinement indicators: strain energy density gradient (left) and vonMises stress (right), both for 7 levels of adaptive refinement iterations.

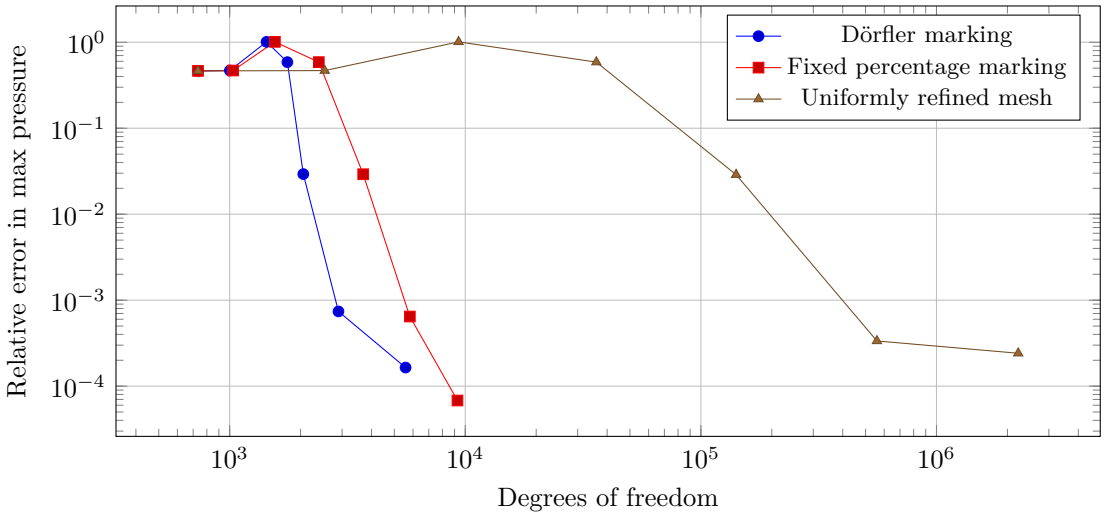

Figure 12: Convergence comparison between our marking strategies: Fixed percentage, Dörfler are tested. Uniformly refined mesh is added as a reference. A faster convergence is observed for the Dörfler strategy.

	Maximum pressure (N/mm^2)				Average time per iteration (sec)			
Degree	2	3	4	5	2	3	4	5
Fully refined TP	502.907	504.608	506.891	507.042	38.98	70.71	117.59	6800
THB-Splines	503.062	504.646	506.903	507.063	1.37	3.52	8.21	14.93
Ad hoc refined TP	504.732	505.08	507.08	507.085	2.90	4.63	9.46	55.58

Table 3: Maximum pressure and average iteration time for all experiments at the finest level of refinement. See also Figure 16 for the number of degrees of freedom used to obtain the results.

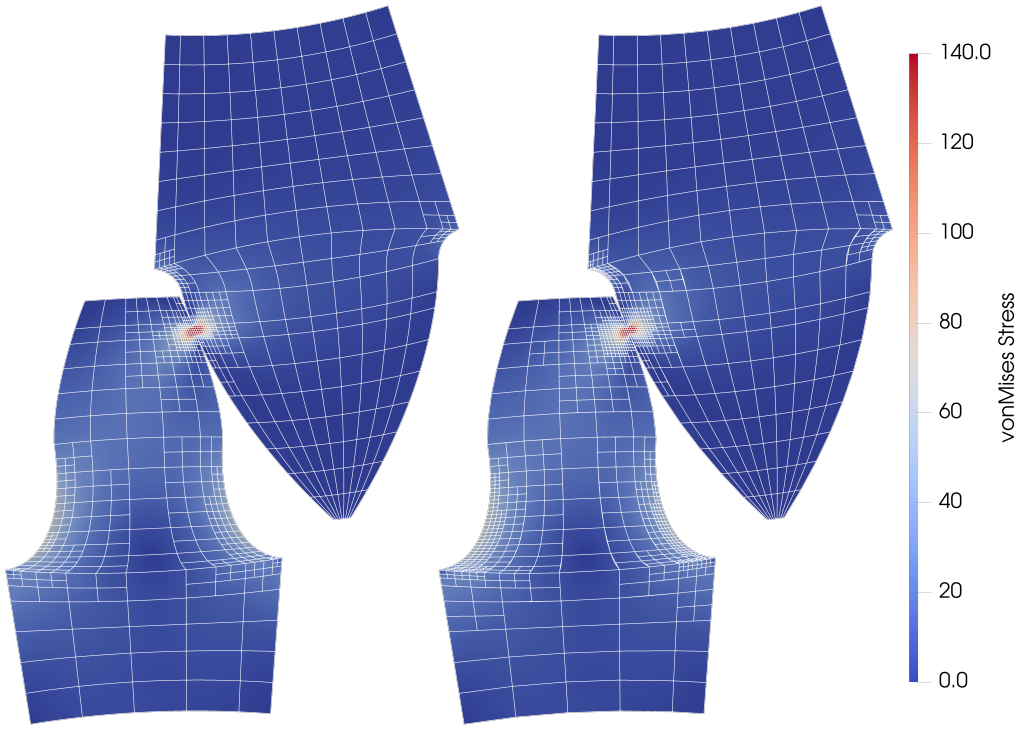

Figure 13: Comparison of THB meshes produced with different refinement strategies, Dörfler (left) and fixed percentage (right), both for 3 levels of adaptive refinement iterations.

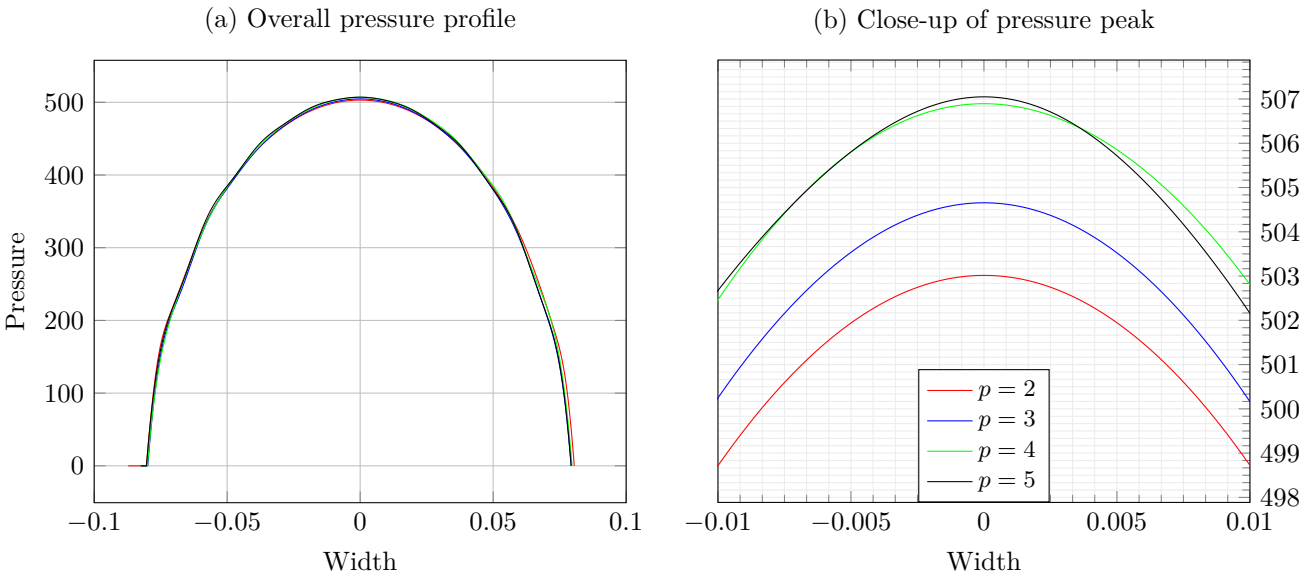

Figure 14: Comparison of pressure profiles for fully refined tensor-product patches of varying degree.

6.6. Computational cost

Lastly, the simulations performed in the previous section, are revisited from a different point of view, that of computational cost. To this end, we consider the finest fully refined tensor product solution as a reference, since it is a parent space of the THB and the *ad hoc* refined splines. Based on that, an assessment of the relative error in maximum pressure versus the number of degrees of freedom at each

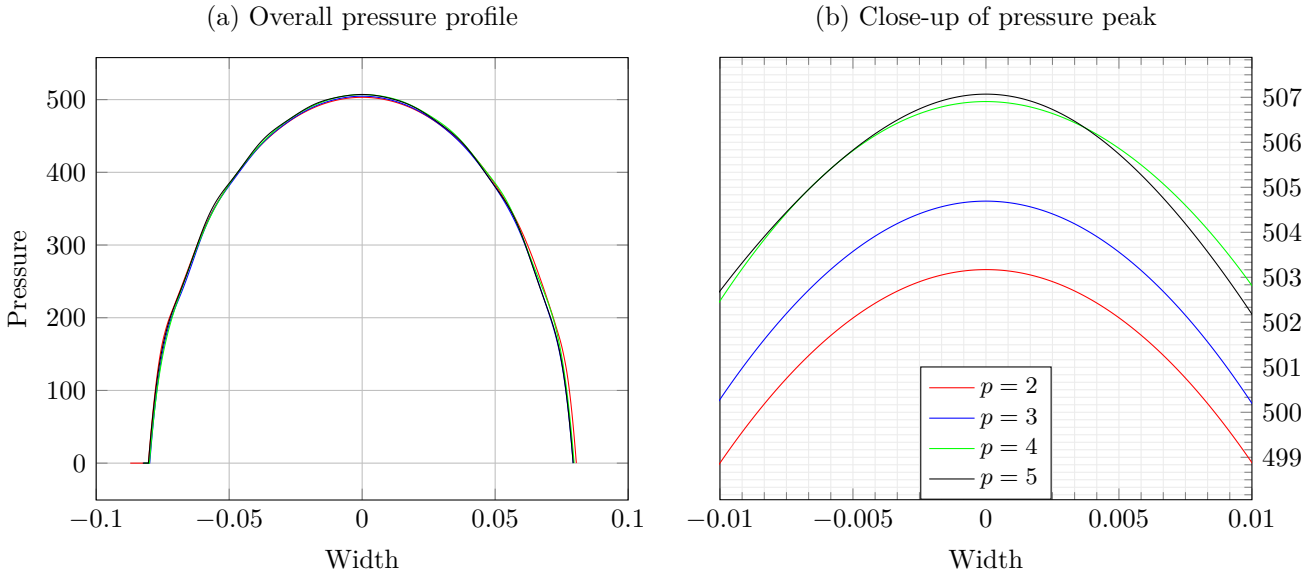

Figure 15: Comparison of pressure profiles for THB-Spline patches of varying degree.

refinement level is performed. The results for polynomial degrees from 2 to 5 are presented in Figure 16. We can observe that THB-Splines consistently achieve better results with far fewer degrees of freedom, with a reduction in most cases by one order of magnitude or more.

It is of particular interest that regardless of degree, the *ad hoc* refined tensor product splines are exhibiting a plateau, where further refining the mesh does not yield a more accurate result. This behaviour is the result of the way the tensor product mesh is constructed. As seen in Figure 7, the *ad hoc* refined tensor product mesh has relatively large elements in the bulk of the tooth, and small elements in the vicinity of the theoretical contact point. Thus the bulk of the tooth deforms differently under the bending load and this results in the deviation in terms of maximum pressure compared to the finest fully refined models. However, the THB discretisation has a much smoother transition from coarse to fine elements since the adaptive refinement acts at the areas where the largest bending strains are present. Due to that, the THB discretisation delivers better results at every refinement step, better approximating the results of the fully refined models.

Finally, to give a feeling of the computation times, in the second part of Table 3 we present the average wall-clock time required for one equilibrium iteration, for each degree at the highest level of refinement. All runs were performed on an Apple M1 Pro CPU with 16GB of memory. It becomes clear that with hierarchical splines, time savings of more than one order of magnitude can be made, while the results remain equally accurate, as we have seen earlier. For a comparison of computational cost between IGA and FEM simulations for the gear contact problem we refer the reader to [15].

7. Conclusions and outlook

Gear contact simulation plays a critical role in the design and analysis of gear systems, which are fundamental components in many mechanical applications such as automotive transmissions, aerospace mechanisms, and industrial machinery. Accurate simulation of gear contact is essential to predict gear performance, durability, noise, and vibration. However, gear contact simulation presents several challenges that may be tackled using the isogeometric analysis paradigm. These include the meshing of complex gear geometry, the robust solution of the nonlinear contact mechanics model as well as the high computational cost in high-resolution models, accounting for contact interactions and other nonlinearities.

Classical splines are lacking the ability to locally refine the mesh and thus the number of degrees of freedom required to accurately resolve the contact region skyrockets, since it is very small compared to the

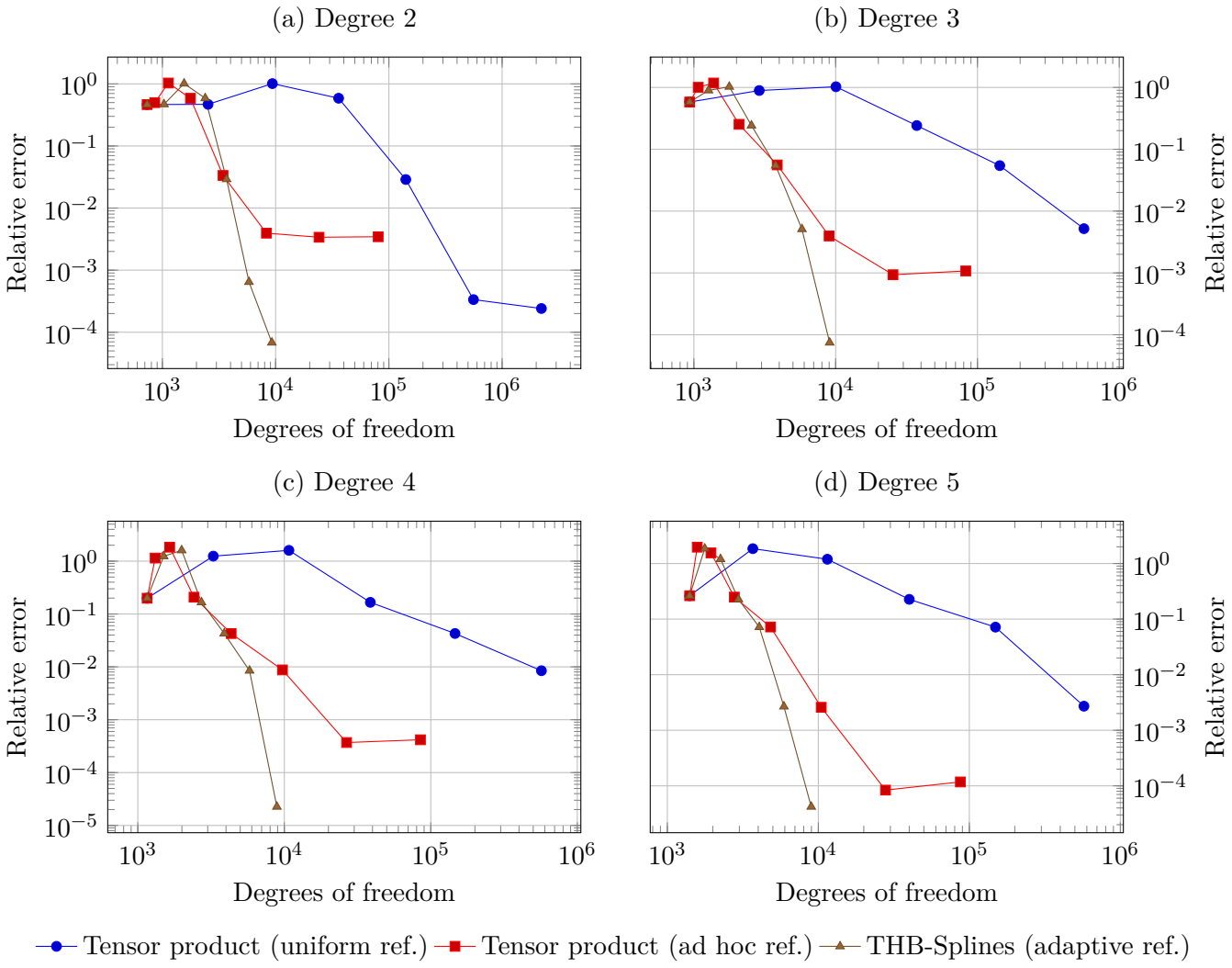

Figure 16: Comparison of relative error in maximum pressure, between globally and *ad hoc* refined tensor product B-Splines and THB-Splines, for polynomial degrees 2 to 5.

overall dimensions of the parts. Truncated hierarchical B-Splines enable this much needed functionality and thus decrease the size of the problem by more than one order of magnitude, as we have shown in our numerical experiments. The validity of the results obtained with THB-Splines has been confirmed by comparing them against those of fully refined tesnor product splines, which span a much larger, parent spline space. Despite the dramatic decrease in degrees of freedom and computation time, a very high agreement with the reference results was observed. Taking advantage of adaptivity, the locally refined THB discretisation is constructed automatically, without exploiting any *a priori* knowledge about the contact point, thus making this methodology generally applicable to all kinds of contact problems. We have shown that adaptive refinement can be driven efficiently by using simple and efficient refinement indicators such as the vonMises stress or the strain energy density gradient, avoiding the computational burden of a posteriori error estimators.

We have demonstrated that the use of THB-Splines of elevated degree and automated adaptive mesh refinement can improve accuracy significantly without excessively increasing computational costs. Overall, gear contact simulation using isogeometric analysis and THB-Splines yields a powerful tool in the design and analysis of gear systems. A careful consideration of the trade-offs involved in the simulation setup

and the choices made in each step of solving, estimating, marking and refining is paramount for successful gear contact analysis.

Potential extensions of our approach include the incorporation of more complex boundary conditions simulation such as natural boundary conditions, which is what is commonly used in real world applications. Also, the extension of this methodology to volumetric splines will enable efficient simulation of three dimensional gears, which have significantly more complex geometry and degrees of freedom. Last but not least, another area of further development is the incorporation of friction in the contact formulation, which will contribute in making the models even more realistic.

Acknowledgements

This paper has received funding from the European Union's Horizon 2020 research and innovation programme under the Marie Skłodowska-Curie grant agreement No. 860843, as well as from BETA CAE Systems.

Appendix A. Gear & Pinion B-Spline patch data.

Detailed geometrical information of the pair of gear teeth referenced in Section 5, is presented in this appendix. Both patches utilise the same bivariate B-Spline basis of degrees (4,2). The knot vector of parametric direction u ($p_u = 4$) is $\Xi_u = [0\ 0\ 0\ 0\ 0\ 1\ 1\ 1\ 1\ 2\ 2\ 2\ 2\ 3\ 3\ 3\ 3\ 3\ ]$ and of direction v ($p_v = 2$) is $\Xi_v = [0\ 0\ 0\ 1\ 1\ 1]$. The patches are illustrated in Figures A.17 and A.18.

Control points are given in Table A.4, in the coordinate system fixed to the center of rotation, with the teeth centered on the y axis. The basis is of size (13,3), and the control points are given in lexicographic order. Starting at the bottom right of the control grid, points are listed consecutively from bottom to top and from right to left.

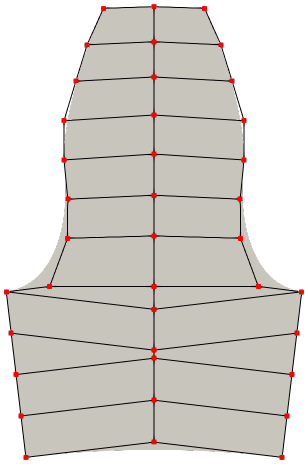

Figure A.17: Gear B-Spline patch and control net.

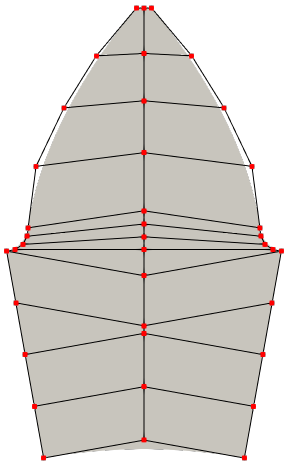

Figure A.18: Pinion B-Spline patch and control net.

Pinion		Gear	
x	y	x	y
4.40011	24.6097	4.70711	39.7221
4.80555	26.8774	4.8873	41.2427
5.21099	29.145	5.06749	42.7633
5.61644	31.4127	5.24769	44.2839
6.02188	33.6803	5.42788	45.8045
5.6574	33.7448	3.83208	46.0011
5.31021	33.9753	3.17662	47.7718
5.1241	34.3337	3.16782	49.2083
5.08008	34.7033	3.30621	50.6485
4.73087	37.3978	3.30851	52.0891
3.50968	39.9621	2.8698	53.5424
2.09245	42.2406	2.45625	54.8808
0.333549	44.338	1.85693	56.2193
0	25.3965	0	40.2799
0	27.7366	0	41.8218
0	30.0767	0	43.3638
0	30.4085	0	43.662
0	32.6036	0	45.1613
0	33.7448	0	46.0011
0	34.3073	0	47.8563
0	34.869	0	49.351
0	35.4469	0	50.8643
0	37.9962	0	52.2993
0	40.2703	0	53.6962
0	42.3442	0	54.9907
0	44.3405	0	56.2807
-4.40011	24.6097	-4.70711	39.7221
-4.80555	26.8774	-4.8873	41.2427
-5.21099	29.145	-5.06749	42.7633
-5.61644	31.4127	-5.24769	44.2839
-6.02188	33.6803	-5.42788	45.8045
-5.6574	33.7448	-3.83208	46.0011
-5.31021	33.9753	-3.17662	47.7718
-5.1241	34.3337	-3.16782	49.2083
-5.08008	34.7033	-3.30621	50.6485
-4.73087	37.3978	-3.30851	52.0891
-3.50968	39.9621	-2.8698	53.5424
-2.09245	42.2406	-2.45625	54.8808
-0.333549	44.338	-1.85693	56.2193

Table A.4: Control points of pinion and gear. All dimensions are in millimetres.

References

[1] S. Glodež, Z. Ren, J. Flašker, Surface fatigue of gear teeth flanks, Computers & Structures 73 (1-5) (1999) 475–483. doi:10.1016/S0045-7949(98)00251-X.

[2] J. Kramberger, M. Šraml, S. Glodež, J. Flašker, I. Potrč, Computational model for the analysis of bending fatigue in gears, Computers & Structures 82 (23-26) (2004) 2261–2269. doi:10.1016/j.compstruc.2003.10.028.

[3] J. Tuma, Transmission and Gearbox Noise and Vibration Prediction and Control, in: M. J. Crocker (Ed.), Handbook of Noise and Vibration Control, 1st Edition, Wiley, 2007, pp. 1086–1095. doi:10.1002/9780470209707.ch88.

[4] F. L. Litvin, A. Fuentes, Gear Geometry and Applied Theory, 2nd Edition, Cambridge University Press, 2004. doi:10.1017/CBO9780511547126.

[5] M. C. Radu, L. Andrei, G. Andrei, A survey on gear meshing quality based on tooth contact analysis, IOP Conf. Ser.: Mater. Sci. Eng. 514 (1) (2019) 012027. doi:10.1088/1757-899X/514/1/012027.

[6] N. L. Pedersen, M. F. Jørgensen, On gear tooth stiffness evaluation, Computers & Structures 135 (2014) 109–117. doi:10.1016/j.compstruc.2014.01.023.

[7] O. D. Mohammed, A Study of Different Considerations to Meet Gear Design Requirements, Procedia Structural Integrity 42 (2022) 1607–1618. doi:10.1016/j.prostr.2022.12.203.

[8] H. Hertz, Ueber die Berührung fester elastischer Körper., Journal für die reine und angewandte Mathematik 1882 (92) (1882) 156–171. doi:10.1515/crll.1882.92.156.

[9] S. M. S. Mukras, Computer Simulation/Prediction of Wear in Mechanical Components, Advances in Tribology 2020 (2020) e8867351. doi:10.1155/2020/8867351.

[10] C. G. Provatidis, Precursors of Isogeometric Analysis: Finite Elements, Boundary Elements, and Collocation Methods, Vol. 256 of Solid Mechanics and Its Applications, Springer International Publishing, Cham, 2019. doi:10.1007/978-3-030-03889-2.

[11] T. Hughes, J. Cottrell, Y. Bazilevs, Isogeometric analysis: CAD, finite elements, NURBS, exact geometry and mesh refinement, Computer Methods in Applied Mechanics and Engineering 194 (39-41) (2005) 4135–4195. doi:10.1016/j.cma.2004.10.008.

[12] D. M. Neto, M. C. Oliveira, L. F. Menezes, Surface Smoothing Procedures in Computational Contact Mechanics, Arch Computat Methods Eng 24 (1) (2017) 37–87. doi:10.1007/s11831-015-9159-7.

[13] L. De Lorenzis, P. Wriggers, T. J. Hughes, Isogeometric contact: A review, GAMM-Mitteilungen 37 (1) (2014) 85–123. doi:10.1002/gamm.201410005.

[14] S. K. Das, S. S. Gautam, A Systematic Review of Isogeometric Contact Analysis and Its Applications, Arch Computat Methods Eng (Apr. 2024). doi:10.1007/s11831-024-10111-9.

[15] C. Karampatzakis, A. Mihailidis, A. Mantzaflaris, C. Provatidis, Contact simulation of tooth flanks using Isogeometric Analysis, in: VDI Wissensforum GmbH (Ed.), International Conference on Gears 2023, VDI Verlag, 2023, pp. 413–428. doi:10.51202/9783181024225-413.

[16] L. Chen, C. Hao, Z. Wang, W. Feng, Y. Yang, Isogeometric Analysis of Gear with Single Tooth Contact, Journal of Mechanical Engineering 57 (3) (2021) 107. doi:10.3901/JME.2021.03.107.

[17] L. Chen, Y. Yu, Y. Shang, Z. Wang, J. Zhang, Application of Isogeometric Analysis Method in Three-Dimensional Gear Contact Analysis, CMES 139 (1) (2024) 817–846. doi:10.32604/cmes.2023.031595.

[18] F. Greco, A. Rosolen, L. Coox, W. Desmet, Contact mechanics with maximum-entropy meshfree approximants blended with isogeometric analysis on the boundary, Computers & Structures 182 (2017) 165–175. doi:10.1016/j.compstruc.2016.11.008.

[19] İ. Temizer, C. Hesch, Hierarchical NURBS in frictionless contact, Computer Methods in Applied Mechanics and Engineering 299 (2016) 161–186. doi:10.1016/j.cma.2015.11.006.

[20] R. Dimitri, L. De Lorenzis, M. Scott, P. Wriggers, R. Taylor, G. Zavarise, Isogeometric large deformation frictionless contact using T-splines, Computer Methods in Applied Mechanics and Engineering 269 (2014) 394–414. doi:10.1016/j.cma.2013.11.002.

[21] T. W. Sederberg, J. Zheng, A. Bakenov, A. Nasri, T-splines and T-NURCCs, ACM Trans. Graph. 22 (3) (2003) 477–484. doi:10.1145/882262.882295.

[22] A. Buffa, G. Gantner, C. Giannelli, D. Praetorius, R. Vázquez, Mathematical Foundations of Adaptive Isogeometric Analysis, Arch Computat Methods Eng 29 (7) (2022) 4479–4555. doi:10.1007/s11831-022-09752-5.

[23] Q. He, T. Yu, L. Van Lich, T. Q. Bui, Thermal buckling adaptive multi-patch isogeometric analysis of arbitrary complex-shaped plates based on locally refined NURBS and Nitsche's method, Thin-Walled Structures 169 (2021) 108383. doi:10.1016/j.tws.2021.108383.

[24] J. Gu, T. Yu, L. Van Lich, T.-T. Nguyen, T. Q. Bui, Adaptive multi-patch isogeometric analysis based on locally refined B-splines, Computer Methods in Applied Mechanics and Engineering 339 (2018) 704–738. doi:10.1016/j.cma.2018.04.013.

[25] I. Malik, An adaptive contact formulation for Isogeometric Finite Element Analysis, Ph.D. thesis, Bauhaus-Universität Weimar (2022). doi:10.25643/BAUHAUS-UNIVERSITAET.4612.

[26] N. Nguyen-Thanh, W. Li, J. Huang, N. Srikanth, K. Zhou, An adaptive isogeometric analysis meshfree collocation method for elasticity and frictional contact problems, Numerical Meth Engineering 120 (2) (2019) 209–230. doi:10.1002/nme.6132.

[27] J. C. Simo, P. Wriggers, R. L. Taylor, A perturbed Lagrangian formulation for the finite element solution of contact problems, Computer Methods in Applied Mechanics and Engineering 50 (2) (1985) 163–180. doi:10.1016/0045-7825(85)90088-X.

[28] L. De Lorenzis, J. Evans, T. Hughes, A. Reali, Isogeometric collocation: Neumann boundary conditions and contact, Computer Methods in Applied Mechanics and Engineering 284 (2015) 21–54. doi:10.1016/j.cma.2014.06.037.

[29] M. E. Matzen, T. Cichosz, M. Bischoff, A point to segment contact formulation for isogeometric, NURBS based finite elements, Computer Methods in Applied Mechanics and Engineering 255 (2013) 27–39. doi:10.1016/j.cma.2012.11.011.

[30] L. Taylor, P. Papadopoulos, On a patch test for contact problems in two dimensions., in: P. Wriggers (Ed.), Nonlinear Computational Mechanics, Springer, Berlin Heidelberg, 1991, pp. 690–702.

[31] İ. Temizer, P. Wriggers, T. Hughes, Contact treatment in isogeometric analysis with NURBS, Computer Methods in Applied Mechanics and Engineering 200 (9-12) (2011) 1100–1112. doi:10.1016/j.cma.2010.11.020.

[32] L. De Lorenzis, İ. Temizer, P. Wriggers, G. Zavarise, A large deformation frictional contact formulation using NURBS-based isogeometric analysis, Numerical Meth Engineering 87 (13) (2011) 1278–1300. doi:10.1002/nme.3159.

[33] L. Mattei, F. Di Puccio, Frictionless vs. Frictional Contact in Numerical Wear Predictions of Conformal and Non-conformal Sliding Couplings, Tribol Lett 70 (4) (2022) 115. doi:10.1007/s11249-022-01657-5.

[34] P. Wriggers, Computational Contact Mechanics, 2nd Edition, Springer, Berlin ; New York, 2006.

[35] D. Graillet, J.-P. Ponthot, L. Stainier, Augmented Lagrangian procedure for implicit computation of contact-impact between deformable bodies., International Journal of Crashworthiness 6 (2) (2001) 209–222. doi:10.1533/cras.2001.0173.

[36] J. Lu, Isogeometric contact analysis: Geometric basis and formulation for frictionless contact, Computer Methods in Applied Mechanics and Engineering 200 (5) (2011) 726–741. doi:10.1016/j.cma.2010.10.001.

[37] C. Giannelli, B. Jüttler, H. Speleers, THB-splines: The truncated basis for hierarchical splines, Computer Aided Geometric Design 29 (7) (2012) 485–498. doi:10.1016/j.cagd.2012.03.025.

[38] T. Dokken, T. Lyche, K. F. Pettersen, Polynomial splines over locally refined box-partitions, Computer Aided Geometric Design 30 (3) (2013) 331–356. doi:10.1016/j.cagd.2012.12.005.

[39] J. Deng, F. Chen, X. Li, C. Hu, W. Tong, Z. Yang, Y. Feng, Polynomial splines over hierarchical T-meshes, Graphical Models 70 (4) (2008) 76–86. doi:10.1016/j.gmod.2008.03.001.

[40] A. V. Vuong, C. Giannelli, B. Jüttler, B. Simeon, A hierarchical approach to adaptive local refinement in isogeometric analysis, Computer Methods in Applied Mechanics and Engineering 200 (49) (2011) 3554–3567. doi:10.1016/j.cma.2011.09.004.

[41] C. Giannelli, B. Jüttler, Bases and dimensions of bivariate hierarchical tensor-product splines, Journal of Computational and Applied Mathematics 239 (2013) 162–178. doi:10.1016/j.cam.2012.09.031.

[42] D. Mokriš, B. Jüttler, C. Giannelli, On the completeness of hierarchical tensor-product B-splines, Journal of Computational and Applied Mathematics 271 (2014) 53–70. doi:10.1016/j.cam.2014.04.001.

[43] P. Hild, S. Nicaise, Residual *a posteriori* error estimators for contact problems in elasticity, ESAIM: M2AN 41 (5) (2007) 897–923. doi:10.1051/m2an:2007045.

[44] L. Song, Y. Hou, Z. Cai, Recovery-based error estimator for stabilized finite element methods for the Stokes equation, Computer Methods in Applied Mechanics and Engineering 272 (2014) 1–16. doi:10.1016/j.cma.2014.01.004.

[45] C. Anitescu, M. N. Hossain, T. Rabczuk, Recovery-based error estimation and adaptivity using high-order splines over hierarchical T-meshes, Computer Methods in Applied Mechanics and Engineering 328 (2018) 638–662. doi:10.1016/j.cma.2017.08.032.

[46] G. Kuru, C. Verhoosel, K. Van Der Zee, E. Van Brummelen, Goal-adaptive Isogeometric Analysis with hierarchical splines, Computer Methods in Applied Mechanics and Engineering 270 (2014) 270–292. doi:10.1016/j.cma.2013.11.026.

[47] K. Van Der Zee, C. Verhoosel, Isogeometric analysis-based goal-oriented error estimation for free-boundary problems, Finite Elements in Analysis and Design 47 (6) (2011) 600–609. doi:10.1016/j.finel.2010.12.013.

[48] Y. Luo, U. Häussler-Combe, An Adaptivity Procedure Based on the Gradient of Strain Energy Density and its Application in Meshless Methods, in: T. J. Barth, M. Griebel, D. E. Keyes, R. M. Nieminen, D. Roose, T. Schlick, M. Griebel, M. A. Schweitzer (Eds.), Meshfree Methods for Partial Differential Equations, Vol. 26, Springer Berlin Heidelberg, Berlin, Heidelberg, 2003, pp. 267–279. doi:10.1007/978-3-642-56103-0_18.

[49] W. Dörfler, A Convergent Adaptive Algorithm for Poisson's Equation, SIAM J. Numer. Anal. 33 (3) (1996) 1106–1124. doi:10.1137/0733054.

[50] C. Giannelli, B. Jüttler, S. K. Kleiss, A. Mantzaflaris, B. Simeon, J. Špeh, THB-splines: An effective mathematical technology for adaptive refinement in geometric design and isogeometric analysis, Computer Methods in Applied Mechanics and Engineering 299 (2016) 337–365. doi:10.1016/j.cma.2015.11.002.

[51] M. Åkerblom, Gear Noise and Vibration A Literature Survey, 2001.

[52] F. Higuchi, S. Gofuku, T. Maekawa, H. Mukundan, N. M. Patrikalakis, Approximation of involute curves for CAD-system processing, Engineering with Computers 23 (3) (2007) 207–214. doi:10.1007/s00366-007-0060-3.

[53] M. A. Lopez, R. T. Wheway, A Method for Determining the AGMA Tooth Form Factor from Equations for the Generated Tooth Root Fillet, Journal of Mechanisms, Transmissions, and Automation in Design 108 (2) (1986) 270–279. doi:10.1115/1.3260813.

[54] T.-R. Wang, N. Liu, L. Yuan, K.-X. Wang, X.-J. Sheng, Iterative Least Square Optimization for the Weights of NURBS Curve, Mathematical Problems in Engineering 2022 (2022) 1–12. doi:10.1155/2022/5690564.

[55] A. Mantzaflaris, An Overview of Geometry Plus Simulation Modules, in: D. Slamanig, E. Tsigaridas, Z. Zafeirakopoulos (Eds.), Mathematical Aspects of Computer and Information Sciences, Vol. 11989, Springer International Publishing, Cham, 2020, pp. 453–456. doi:10.1007/978-3-030-43120-4_35.

[56] DIN 51354-1:1990-04, Testing of lubricants; FZG gear test rig; general working principles (Apr. 1990).